AIAA JOURNAL
Vol. 57, No. 4, April 2019

Theoretical Prediction of Roll Moment Due to Sideslip for Thin Low-Aspect-Ratio Wings

Thomas Linehan* and Kamran Mohseni†
University of Florida, Gainesville, Florida 32611-6250

DOI: 10.2514/1.J057160

The physics associated with leading-edge flow reattachment and tip vortex roll-up in crossflow are incorporated into a simple theory that enables the improved prediction of the lateral static stability derivative C_{l_β} of thin low-aspect-ratio wings at low Reynolds numbers. The theory is validated against experimental stability derivative measurements of a total of 13 flat-plate wings. Accurate prediction of C_{l_β} is obtained to lift coefficients as high as 0.7. Results indicate that the tip vortex, and its expedited roll-up over thin low-aspect-ratio wings at low Reynolds numbers, is destabilizing in terms of C_{l_β}. In addition, leading-edge flow reattachment at low lift coefficients, whether in the form of a separation bubble for wings with unswept leading edges or an elongated separation region on wings with swept leading edges, may be stabilizing or destabilizing in terms of C_{l_β} based on whether the wing has forward or backward quarter-chord sweep.

Nomenclature

$\mathcal{AR}$	=	aspect ratio; b^2/S
b	=	wingspan
C_L	=	lift coefficient
C_l	=	roll moment coefficient
C_{l_β}	=	lateral static stability derivative, rad^{-1}
c_t	=	tip chord
c	=	root chord
q	=	dynamic pressure
Re	=	Reynolds number based on root chord
S	=	wing area
U_∞	=	freestream velocity
$\bar{y}$	=	lateral center of pressure
α	=	angle of attack, deg
β	=	sideslip angle, deg
Γ	=	characteristic circulation
Λ	=	quarter-chord sweep angle
λ	=	taper ratio; c_t/c
ρ	=	density of air

Superscript

$*$	=	nondimensional through division by $b/2$

I. Introduction

LOW-LEVEL control of fixed-wing unmanned aerial vehicles (UAVs) requires regulating aircraft rolling moment at a wide range of operational points. This consists of flight segments associated with takeoff, climb, cruise, loiter, descent, recovery, and maneuvering flight, to name a few. Within this flight profile, the aircraft may experience fully attached and/or separated flow over its lifting surfaces while being subject to energetic background flows, such as atmospheric wind gusts, the turbulent airwake of an aircraft carrier, neighboring aircraft, and buildings as in urban flight. Across these flow regimes and these flight conditions, an accurate knowledge of the aircraft's lateral dynamics is imperative for mission success.

Modeling the aircraft dynamics during unaccelerated flight at low "attached-flow" angles of attack and high Reynolds numbers is the hallmark of classical aircraft mechanics. In this flight regime, low-order potential flow methods such as lifting-line methods for high-$\mathcal{AR}$ lifting surfaces and lifting surface and vortex lattice methods for low-$\mathcal{AR}$ lifting surfaces have been shown to accurately predict the dynamics of aircraft under small disturbances. Although there have been new developments in these fields such as incorporating unsteady effects associated with wind gusts and wing deformations [1], generally these methods neglect viscous effects associated with separated flows and therefore are not equipped to predict the dynamics of aircraft during large-amplitude maneuvers and high-angle-of-attack flight. Moreover, as will be shown next, these methods are unable to predict the lateral dynamics of thin low-$\mathcal{AR}$ wings at low Reynolds numbers even during operation at low angles of attack, which becomes important in light of recent trends toward the miniaturization of fixed-wing UAVs.

To exemplify the breakdown of classical vortex models for thin low-$\mathcal{AR}$ wings at low Reynolds numbers, consider the classical Weissinger vortex arrangement [2] in Fig. 1 used to model rectangular wing in sideslip. Weissinger placed an infinite series of skewed, horseshoelike vortices along the $c/4$ line, where each vortex element in the vortex system consists of a $c/4$ vortex, chordwise bound vortices, and trailing vortices. The bound vortices stem from the $c/4$ line and extend along the chord to the trailing edge of the wing. The trailing vortices begin at the wing's trailing edge and extend to downstream in the direction of the freestream velocity U_∞.

Using this vortex model, Weissinger employed the Kutta–Joukowski theorem to obtain a linear equation for the lateral static stability derivative $C_{l_\beta} \equiv (\partial C_l/\partial\beta)$ as a function of lift coefficient C_L. Here, C_l is the roll moment coefficient, and β is the sideslip angle defined as $\beta \equiv \sin(v/U_\infty)^{-1}$, where v is the crossflow velocity defined positive out the right wing. The derivative C_{l_β} is commonly referred to as the "dihedral derivative" because, upon satisfying the stability criteria $C_{l_\beta} < 0$, a stabilizing roll moment is generated in the presence of crosswind, which would drive the aircraft toward wing's level flight. The slope obtained by Weissinger, or $(C_{l_\beta}/C_L)_{\text{Weissinger}}$, is

$$\left(\frac{C_{l_\beta}}{C_L}\right)_{\text{Weissinger}} = -\frac{\kappa}{\mathcal{AR}}\left[\frac{0.71\lambda + 0.29}{1+\lambda}\right] + 0.05 \tag{1}$$

where $\mathcal{AR}$ and λ are the aspect ratio and taper ratio of the wing, respectively. The theory of Weissinger fixes the value of κ to 1.5; however, it was noted that a κ value of 1 was more accurate when comparing with experiments of wings tested at the time. The lateral static stability of the unswept wing was shown to stem solely from the

Received 1 February 2018; revision received 8 October 2018; accepted for publication 28 November 2018; published online 6 March 2019.

*Graduate Research Assistant, Department of Mechanical and Aerospace Engineering. Student Member AIAA.

†William P. Bushnell Endowed Professor, Department of Mechanical and Aerospace Engineering, Institute for Networked Autonomous Systems. Associate Fellow AIAA.

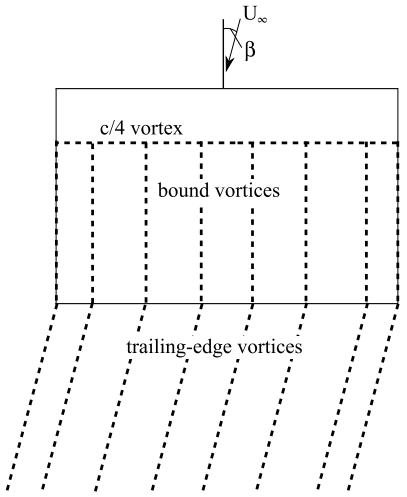

Fig. 1 Weissinger vortex arrangement for the rectangular wing in sideslip.

chordwise bound vortices under the small sideslip assumption. Modifying the vortex representation of Weissinger to incorporate the effects of quarter-chord sweep angle Λ, Queijo [3] recovered an equation for the slope C_{l_β}/C_L using a similar methodology. The theory of Queijo is

$$\left(\frac{C_{l_\beta}}{C_L}\right)_{\text{Queijo}} = -\frac{1}{2}\left[\frac{3}{\mathcal{AR}(1+\lambda)} + \bar{y}^*\left[\tan(\Lambda) - \frac{6}{\mathcal{AR}}\left(\frac{1-\lambda}{1+\lambda}\right)\right]\right] + 0.05 \tag{2}$$

which reduces to that of Weissinger [Eq. (1)] with $\kappa = 1.5$ for rectangular wings ($\Lambda = 0$ deg, $\lambda = 1$).

The Queijo and Weissinger theories [Eqs. (1) and (2)] were shown to be in good agreement with both low-$\mathcal{AR}$ and high-$\mathcal{AR}$ wings at high Reynolds numbers. This is exhibited in Fig. 2, which displays the slope C_{l_β}/C_L as a function of $\mathcal{AR}$ for rectangular wings as predicted by Eq. (2) and compared with the high-Reynolds-number experiments of Goodman and Brewer [4] and Letko and Goodman [5] on thick rectangular wings with NACA 0012 and NACA 2312 airfoils, respectively. However, when compared with recent low-Reynolds-number experiments ($Re \approx 75{,}000$) by the authors [6] on thin (thickness-to-chord ratio <6%) flat-plate rectangular wings with a 5:1 elliptical leading-edge profile, the predicted slope C_{l_β}/C_L is nearly double that of the measured value for the tested wings.

The breakdown of the vortex representation and accompanying theory of Weissinger and Queijo for C_{l_β}/C_L can be deciphered immediately when comparing Figs. 1 and 3, where Fig. 3 displays smoke-wire visualizations of Shields and Mohseni [7] on an $\mathcal{AR} = 1$

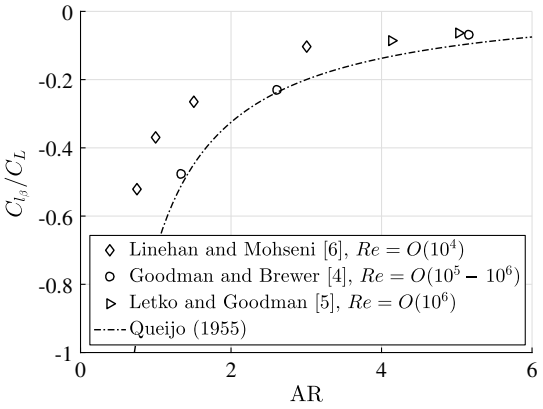

Fig. 2 Experimental measurements of the stability ratio C_{l_β}/C_L as a function of aspect ratio $\mathcal{AR}$ for rectangular wings in comparison with the theory of Queijo [3] [Eq. (2)].

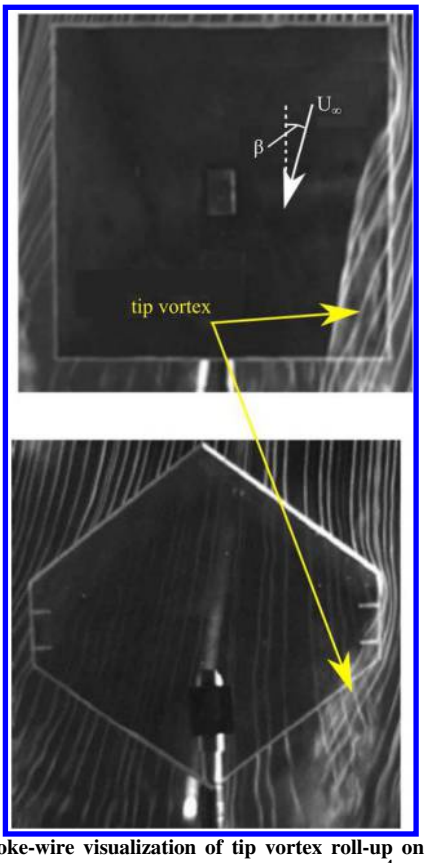

Fig. 3 Smoke-wire visualization of tip vortex roll-up on sideslipped low-$\mathcal{AR}$ wings. $\alpha = 10$ deg, $\beta = 10$ deg, $Re = 7.5 \times 10^4$.

rectangular (Fig. 3a) and $\mathcal{AR} = 1.6$ swept-tapered (Fig. 3b) wing at a sideslip angle $\beta = 10$ deg and angle of attack $\alpha = 10$ deg. The thickness-to-chord ratio was 3% for these wings, and the Reynolds number based on the root chord was 75,000. From Fig. 3, the separated side-edge shear layer rolls up over the wing to form a recognizable tip vortex, which is oriented in the direction of the freestream velocity. These physics are not accounted for by the Weissinger lifting-line-type vortex model nor conventional lifting-surface or vortex lattice methods, in which chordwise-oriented bound vortices are still placed near the windward wing's side-edge in sideslip.

The preceding case illustrates that, to accurately model the lateral dynamics of thin wings at low Reynolds numbers, one must acknowledge the effects of separated flows over the wing. In recent years, there has been substantial progress in characterizing and modeling separated flows to improve the prediction of aircraft dynamics at low speeds. Investigations in this regard branch out into two main research areas distinguished by whether the dynamics are treated as steady or unsteady. To limit the scope of this work, we focus on the influence of separated flow on steady flight at low Reynolds numbers. Therefore, this work mainly pertains to fixed-wing aircraft during flight segments involving climb, cruise, loitering, and descend. In regard to the treatment of unsteady dynamics involving separated flows, interested readers are referred to the work in the following Refs. [8–14] among many others.

During steady flight at low-to-moderate angles of attack, separation occurs from the leading and side edges of the thin wing. The separation and subsequent roll-up of the separated side-edge shear layer forms the tip vortex, which grows in size and strength with increasing lift. Unlike the tip vortex, the organization of leading-edge vorticity goes through various developmental stages from low to high angle of attack [6]. At low Reynolds numbers in the range $\mathcal{O}(10^4) - \mathcal{O}(10^5)$, the leading-edge flow at low angles of attack may separate and transition over the wing, forming a separation bubble. At higher angles of attack, the leading-edge vorticity tends to roll-up over the wing, forming transitional vortices that shed downstream into the wake aperiodically. At even higher angles of attack, wings of

sufficiently low aspect ratio experience a stable recirculation of leading-edge vorticity over the wing and an attenuation of downstream vortex shedding. Operating an aircraft at each of these flight conditions changes the aircraft's lateral and longitudinal response in ways that are only beginning to be explored.

Often an understanding of how certain key flow features on the wing (such as the tip vortex and the separation bubble) affect the dynamics of the aircraft can be useful when developing new predictive models. Over the years, the tip vortex and separation bubble have become readily understood for their impacts on the longitudinal performance and stability of the wing. For example, the separation bubble is recognized to degrade both airfoil [15,16] and wing performance [17–19], whereas the additional lift associated with the tip vortex is noted to attenuate this effect specifically for low-aspect-ratio wings [20–25]. The tip vortex has also been recognized to increase pitch stability [19,23,25] and to both increase lift and delay stall due to its interaction with leading-edge flow [26,27].

More recently, the separated flows around the leading edge and side edge of the wing have been investigated for their effects on the lateral stability of wings at low Reynolds numbers. The free-to-roll experiments of Gresham et al. [28,29] on rectangular, elliptical, and Zimmerman wings of $\mathcal{AR} = 2$ revealed undesired roll oscillations, or "wing rock", notably at angles of attack before stall. The oscillations were noted to be driven by time-lag effects in the strength of the tip vortices. Methods such as acoustic forcing [30], synthetic jet excitation [31], and wing-tip bleed [32] have recently been shown to suppress these oscillations. The tip vortex was also postulated as the source of the strong coupling of roll moment and angle of attack on sideslipped, low-$\mathcal{AR}$ wings and the large stabilizing lateral static stability derivative C_{l_β} at nominal trim angles [33]. The effects of the tip vortex were shown to be passively mitigated by using a low-taper-ratio wing or using end plates [34]. The stability cross-coupling of roll moment and angle of attack was shown to result in new stability modes such as "roll resonance" [35], which may result in roll departure. At high angles of attack, the coupling of roll moment and angle of attack for the sideslipped wing becomes nonlinear where the magnitude of roll moment "stalls" notably at an angle of attack below that of lift stall [33]. Linehan and Mohseni [6] directly measured the three-dimensional flow in this nonlinear regime, revealing that the formation of the recirculating leading-edge separation region at high angles of attack was destabilizing in terms of C_{l_β}. Moreover, this work revealed that, for low-$\mathcal{AR}$ rectangular wings, the flow stalls from the wing tips inward, which is an unfavorable handling quality near stall and notably opposite to the favorable stall characteristics for high-$\mathcal{AR}$ rectangular wings, where stall progresses from the midspan outward.

In terms of the modeling of roll moments generated by low-$\mathcal{AR}$ wings, recently a vortex model was developed by DeVoria and Mohseni [36] to predict lift, drag, and roll moment, which accounted for the effects of edge separation over the wing. In this work, DeVoria and Mohseni theoretically derived a parabolic spanwise loading distribution for rectangular wings using potential flow methods due to the reattached leading-edge flow. The model was shown to accurately predict lift and drag and provide fair prediction of roll moment for rectangular wings in sideslip.

Even with the current knowledge of the stability of low-$\mathcal{AR}$ wings at low Reynolds numbers, the impact of the tip vortex and leading-edge flow reattachment on the roll stability of these wings is not clear and, as will be shown in this paper, often nonintuitive. For example, Shields and Mohseni [33] presumed that the tip vortex asymmetry over the wing (see Fig. 3) is responsible for the large stabilizing roll moments in sideslip on low-$\mathcal{AR}$ wings. In this work, we show the opposite to be true, where the tip vortex asymmetry on the wing actually reduces the lateral stability of the wing.

Therefore, the aim of this work is to understand the effects of the tip vortex and leading-edge flow reattachment on C_{l_β} and incorporate these effects into a model that improves C_{l_β} prediction of thin low-$\mathcal{AR}$ wings at low Reynolds numbers. To accomplish this, experimental stability derivative measurements are made on a total of 13 low-aspect-ratio swept and tapered wings at low Reynolds numbers. The C_{l_β} curves are characterized in detail for two representative wings with the assistance of particle image velocimetry measurements and surface oil-flow visualizations. The purpose here is to diagnose the impact of leading-edge flow reattachment on the trends between C_{l_β} and C_L for these wings, as was previously done for rectangular wings. Based on this analysis, we propose a new vortex model that more accurately represents the flow physics and derive a new linear theory for C_{l_β}. To extend prediction of C_{l_β} to higher lift coefficients, a modification is then made to the linear theory to capture the nonlinear effects associated with leading-edge flow reattachment. Ultimately, the theory is shown to accurately predict nonlinear trends in C_{l_β} to lift coefficients as high as $C_L = 0.7$.

The paper is organized as follows. In Sec. II, the wind-tunnel measurement facility and the stability derivative recovery experiment and methodology are outlined. In Sec. III, a characterization of the C_{l_β} curves of two representative swept wings is made. In Sec. IV, the new vortex model is presented followed by the derivation of an analytical equation for C_{l_β}. A discussion of Reynolds number effects is made in Sec. V. Last, Sec. VI incorporates concluding remarks.

II. Experiment and Methodology

A total of 13, flat-plate wings were investigated experimentally in this study. These wings are shown in Table 1 and are organized into wing sets by their taper ratio λ. The dotted line on each wing diagram indicates the quarter-chord line. Wing set 1 contains four rectangular wings of aspect ratio $\mathcal{AR}$ ranging from 0.75 to 3, with thickness-to-chord ratios ranging from 2.8 to 6.6%. The data for these wings are replotted from Linehan and Mohseni [6]. The experiments in [6] were conducted in the same experimental facility as the current study.

Wing sets 2–4 can be inscribed in a 15.24×15.24 cm square and maintained a combined taper ratio and aspect ratio of $\lambda = 0.75$ and $\mathcal{AR} = 1.14$; $\lambda = 0.5$ and $\mathcal{AR} = 1.33$; and $\lambda = 0.25$ and $\mathcal{AR} = 1.6$, respectively. The thickness-to-chord ratio of these wings was 3%. Within wing sets 2–4, the quarter-chord sweep angle Λ was varied as tabulated. One can organize these wings also by leading- and trailing-edge sweep angles. Analyzing the columns of the schematics of wing sets 2–4, wings in the column A had a variable trailing-edge sweep angle with a fixed and unswept leading edge. Swept wings in column B had a leading and trailing-edge sweep angle that was varied in equal amounts. Load measurements of these wings are replotted from Shields and Mohseni [33]. These measurements were taken in a different experimental facility from the current study. Last, the swept wings in column C had a variable leading-edge sweep angle with a fixed and unswept trailing edge. All wings in Table 1 had a 5:1 leading-edge profile and square side and trailing edges.

The Reynolds number of the experiments are tabulated in Table 1 and range from 7.15×10^4 to 7.5×10^4. A discussion of Reynolds number effects on lateral stability derivative measurements at low Reynolds numbers is given in Sec. V.

The experimental facility at the University of Florida consists of an Engineering Laboratory Design recirculating wind tunnel. The test section has a 61×61 cm^2 cross section and is 2.44 m in length. The wind tunnel can achieve freestream velocities ranging from 3 to 91.4 m/s and has a freestream turbulence intensity of 0.12% at the tested speeds. Direct six-component force and moment measurements were made in the ELD tunnel. The details of this experiment are described next.

A. Force and Moment Measurements

Aerodynamic forces and moments on model wings were measured using the Micro-Loading Technologies six-component internal sting force balance, which has been used extensively by our research group [6,33–37]. The angle of attack α and sideslip angle β of the wing were varied using a robotic positioning system [38]. Angle of attack was realized by linearly actuating two vertical rods. Sideslip angle was realized by turntable rotations of a motorized turntable. Images of the measurement and positioning equipment are shown in Fig. 4, which depict the model, sting force balance, positioning system, and associated motor drivers and control system. The errors in angle of attack and sideslip angle positioning were ± 0.2 and ± 1.4 deg, respectively.

Table 1 Experimental parameters of wings in this study

	$\mathcal{R}$	Re_c	c_r, cm	b, cm	λ	Λ, deg
			Set 1			
A	0.75	7.66×10^4	15.24	11.43	1	0
B	1	7.66×10^4	15.24	15.24	1	0
C	1.5	7.15×10^4	12.7	19.05	1	0
D	3	7.72×10^4	6.35	19.05	1	0
			Set 2			
A	1.14	7.5×10^4	15.24	15.24	0.75	−7.1
B	1.14	7.5×10^4	15.24	15.24	0.75	7.1
C	1.14	7.5×10^4	15.24	15.24	0.75	20.6
			Set 3			
A	1.33	7.5×10^4	15.24	15.24	0.5	−14.0
B	1.33	7.5×10^4	15.24	15.24	0.5	14.0
C	1.33	7.5×10^4	15.24	15.24	0.5	36.9
			Set 4			
A	1.6	7.5×10^4	15.24	15.24	0.25	−20.6
B	1.6	7.5×10^4	15.24	15.24	0.25	20.6
C	1.6	7.5×10^4	15.24	15.24	0.25	48.4

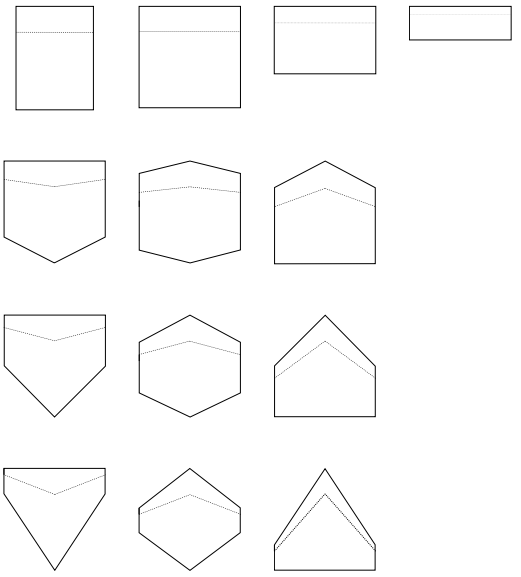

Five sideslip angles were tested for each model: $\beta = -10, -5, 0, 5, 10$. At each sideslip angle, the model was swept through a range of angles of attack $\alpha = -26$–46 deg, in 2 deg increments. Upon movement to the next angle of attack location, data acquisition was halted for 4 s to allow for initial flow transients to subside, after which 16,384 samples were taken on each channel of the force balance at 4096 Hz, resulting in a total sampling time of 4 s. An identical sweep was made beforehand with the wind off, which acted as an inertial "tare" set. Strain-gauge wind-on data were first subtracted from tare data to isolate the aerodynamic loads from the average inertial loads. Tared strain-gauge data were then converted to aerodynamic loads using techniques outlined by the AIAA strain-gauge standard.

The aerodynamic quantities of interest in this paper are lift coefficient $C_L = (2L/\rho U_\infty^2 S)$, roll moment coefficient $C_l = (2l/\rho U_\infty^2 S b)$, and the lateral stability derivative $C_{l_\beta} \equiv \frac{\partial C_l}{\partial \beta}$, where U_∞ is the freestream velocity, ρ is the fluid density, S is the wing area, and b is the wingspan. Estimates of uncertainty for coefficient quantities were obtained by applying the Taylor series method for uncertainty propagation as described in Coleman and Steele [39] to an example test case. The test case was the $\mathcal{R} = 1$ wing at $\beta = -10$ deg and $\alpha = 10$ deg subject to uniform fluid velocity $U_\infty = 7.57$ m/s and constant fluid density $\rho = 1.194$ kg/m^3. The measured lift force L and roll moment l at this condition were 0.297 N and 0.258 N-cm lb-in. Because of the large number of samples, only uncertainties associated with bias errors are considered in this analysis. The absolute bias errors of measured variables U_∞, b, and c are 0.1 m/s, 0.79 mm, and 0.79 mm, respectively. Relative bias errors of l and L are 4.2 and 2.3%, respectively. Bias errors of lift and roll moment were obtained by loading the sting balance with known weights resulting in loads and torques of comparable magnitude to those experimentally measured. The maximum bias error of a set of five repeated known-load experiments is used as the measurement uncertainty for roll moment and lift. The relative and absolute (in parentheses) uncertainties for lift coefficient, roll moment coefficient, and the lateral stability derivative are computed to be 3.5% ($\Delta C_L = 0.0133$), 5.1% ($\Delta C_l = 0.0011$), and 5.2% ($\Delta C_{l_\beta} = 0.0063$), respectively.

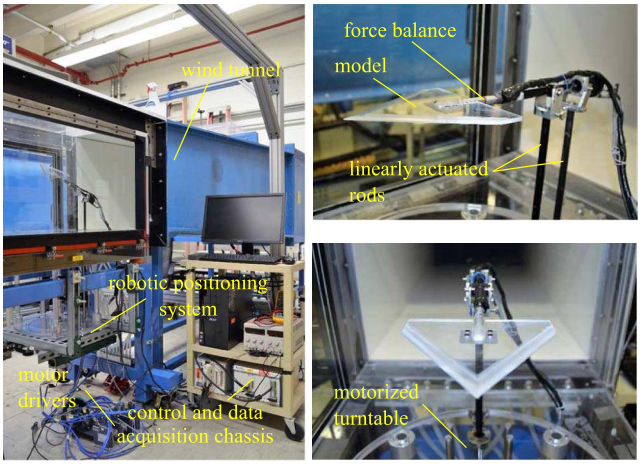

Fig. 4 Experimental facility for stability derivative recovery. Equipment consists of a four-degree-of-freedom robotic positioning system and a six-component strain-gauge force balance.

Blockage effects from streamline curvature, wake, and solid bodies were corrected for based on methods presented by Rae and Pope [40]. Velocity corrections, as a percentage of the freestream velocity, ranged from $\mathcal{O}(10^{-2})$ at $\alpha = 0$ deg to $\mathcal{O}(10^0)$ at $\alpha = 46$ deg. Corrections to angle of attack were generally less than 0.5 deg throughout the tested angle-of-attack range. Coefficient corrections became substantial at high angles of attack. For example, the maximum lift coefficient $C_{L_{\max}}$ and the maximum roll moment coefficient $C_{l_{\max}}$ for the $\mathcal{R} = 1.14$, $\lambda = 0.75$, $\Lambda = -7.1$ deg wing were reduced by 8.3 and 2.1%, respectively. This case represents the largest coefficient correction in $C_{L_{\max}}$ and $C_{l_{\max}}$ out of all wings experimentally tested in this study.

Figure 5 displays representative data for the $\lambda = 0.25$, $\mathcal{R} = 1.6$ backward- and forward-swept wings of sweep angle −20.6 and 48.4 deg, respectively. Lift and roll moment, expressed as coefficients C_L and C_l, respectively, are plotted as a function of angle of attack at all tested sideslip angles. Included in the lift coefficient plots are theoretical predictions of the lift slope for each wing at zero sideslip as obtained from Helmbold's equation [41]:

$$C_{L_\alpha} = \frac{a_0}{\sqrt{1 + (a_0/(\pi \mathcal{R}))^2} + a_0/(\pi \mathcal{R})} \tag{3}$$

where $a_0 = 2\pi$.

From Fig. 5, the lift curve for each wing at low angles of attack remains approximately linear with a slope well approximated by

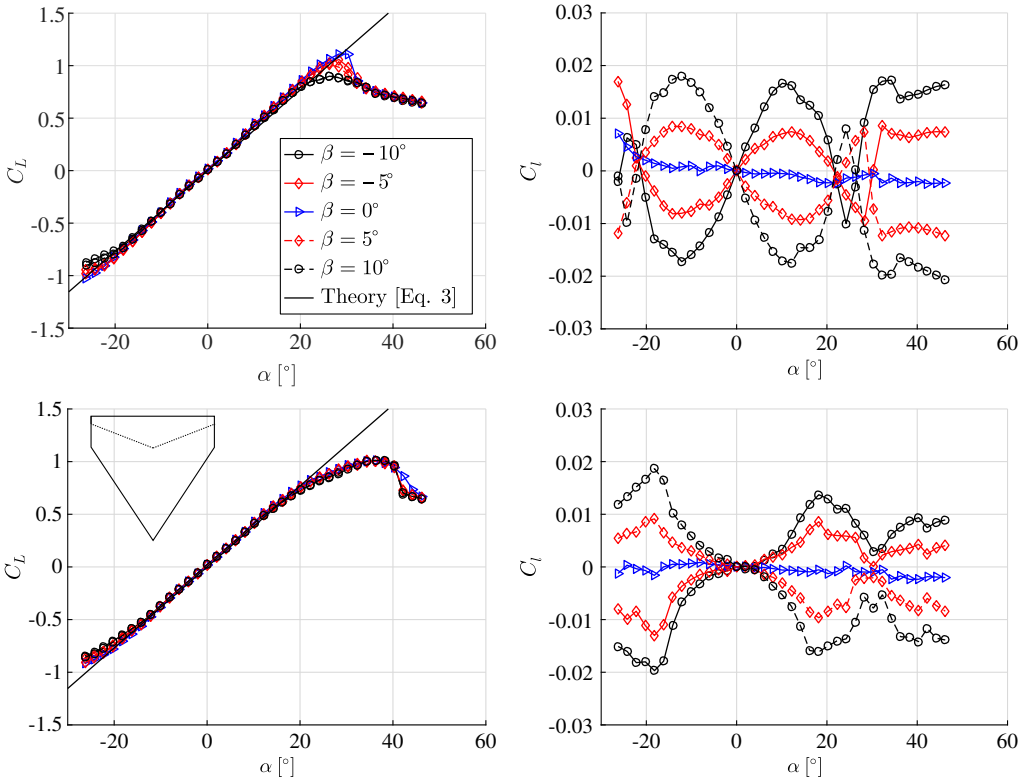

Fig. 5 Lift coefficient (left) and roll moment coefficient (right) as a function of angle of attack for two swept wings of $\mathcal{AR} = 1.6$ and $\lambda = 0.25$ at various sideslip angles. Insets depict planform geometry.

Eq. (3). The effect of sideslip angle on C_L is isolated to high angles of attack near stall. Here, the sensitivity of C_L to sideslip angle differs for each wing. For the backward-swept wing, increasing the magnitude of sideslip reduces prestall lift at angles of attack in the range 18 deg $< \alpha <$ 32 deg and further decreases $C_{L_{\max}}$. In contrast, increasing the magnitude of sideslip of the forward-swept wing reduces lift only at poststall angles of attack $\alpha >$ 40 deg.

In steady sideslip, a lifting wing experiences a roll moment about its midspan due to asymmetric flow over the wing. At positive angles of attack before lift stall for the wings tested in this study, the sign of the roll moment is generally such that a negative sideslip angle produces a positive roll moment and vice versa. This trend is stabilizing because it would assist in driving the aircraft to wings-level flight in real flight. As observed in the roll moment coefficient measurements of Fig. 5, the magnitude of roll moment generated in sideslip is sensitive to the angle of attack, sideslip angle, and the geometry of the wing. The combined sensitivity of roll moment to both angle of attack and sideslip is in stark contrast to lift production of these wings, which is largely insensitive to sideslip (except at high angles of attack near stall). The roll moment curves for each wing at a nonzero sideslip angle exhibit several distinct breaks, or changes in the slope of roll moment with respect to lift coefficient, throughout the tested angle of attack range. Although it is customary for wings to exhibit nonlinear trends in roll moment generation at high angles of attack in sideslip, these trends are usually accompanied by distinct changes in the lift curve slope C_{L_α} because they are attributed to an asymmetric progression of stall over the wing in sideslip. In the current measurements of thin, low-$\mathcal{AR}$ (LAR) wings at low Reynolds numbers, nonlinearities in roll moment curves initiate at low angles of attack $\alpha \approx$ 4–10 deg well below that of lift stall and are accompanied by only minor changes in the lift slope. It is these peculiar trends in the roll moment curves at low angles of attack that motivate the current work.

To further elucidate the trends in roll moment generation in sideslip, the lateral static stability derivative C_{l_β} was computed at each angle of attack by fitting a line to C_l versus β curves at each angle of attack (not shown). Because of the negligible sensitivity of C_L to sideslip angle at angles of attack below lift stall, one can directly plot C_{l_β} as a function of $C_{L,\beta=0\text{ deg}}$, where $C_{L,\beta=0\text{ deg}}$ is the lift coefficient at zero sideslip. Hereafter, we will drop the subscript $\beta = 0$ deg for notational brevity and $C_L = C_{L,\beta=0\text{ deg}}$ unless otherwise noted. Throughout this work, the slope C_{l_β}/C_L as reported is found by fitting a line to the C_{l_β} versus C_L curve at $|\alpha| < 5$ deg or $|C_L| < 0.2$. The slope is computed from C_{l_β} measurements at such low lift coefficients due to the nonlinear effects noted to occur at $|C_L| > 0.2$ specifically, on the swept wings. These nonlinear features are characterized next with the assistance of qualitative and quantitative flow imaging.

III. Characterization of C_{l_β} Curves

Because of the scarcity of low-Reynolds-number stability derivative measurements in the literature, we take the time here to analyze the unique stability trends of the swept tapered wings in Fig. 5. The data previously presented in Fig. 5 can be represented more clearly if $-C_{l_\beta}$ is plotted as a function of C_L as is done in Fig. 6.

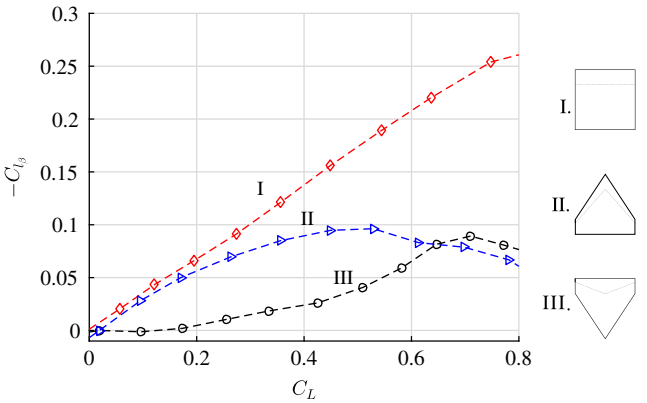

Fig. 6 Lateral static stability curves for wings with planform geometries as indicated.

By plotting $-C_{l_\beta}$, increases along the y axis correspond to increases in the lateral static stability of the wing, indicating that a wing when perturbed in sideslip will generate a restorative roll moment.

The stability curve of the rectangular wing is provided in Fig. 6 for reference. A detailed classification of the low-Reynolds-number stability curve for rectangular wings of low $\mathcal{R}$ was made in previous work by the authors using stereo digital particle image velocimetry [6]. A relevant finding of this work was that, as C_L is increased for sufficiently low-$\mathcal{R}$ wings, there exists a lag (in terms of C_L) between the advancement of leading-edge flow separation and the downwash on the wing. This feature results in highly unsteady transitional leading-edge flow over the wing at initial lift coefficients involving leading-edge separation $C_L \approx 0.35$ because the downwash on the wing is of insufficient strength to steadily reattach such flow back to the wing. However, at higher lift coefficients $C_L > 0.7$, a steadier reattachment of leading-edge flow occurs and a circulatory leading-edge vortex exists on the wing because the tip vortex downwash is sufficient to curb the downstream shedding of leading-edge vorticity. The occurrence of transitional separated flow over the wing at $C_L \approx 0.35$ does not result in a significant change in the slope $-C_{l_\beta}/C_L$ in this lift coefficient range for the rectangular wing (see Fig. 6). It is only at very high lift coefficients $C_L > 0.7$ for which the C_{l_β} curves begin to behave nonlinearly due to the occurrence of recirculatory flow over the wing.

Although the stability curve of the unswept wing remains linear up until a lift coefficient $C_L \approx 0.7$, the swept wings experience a distinct change in slope C_{l_β}/C_L, or "break", in their stability curves at lift coefficients $C_L \approx 0.2$ and $C_L \approx 0.5$. Similar observations were made by Polhamus and Sleeman, Jr., [42] in terms of the difference in the lift coefficient corresponding to breaks in the C_{l_β} curves between unswept and swept wings. However, tests in that work were conducted at higher Reynolds numbers $Re = 10^5 - 10^6$, and the lift coefficients of the breaks were substantially higher than in the current study. For example, the swept wing in the Polhamus and Sleeman, Jr., study experienced the first break at $C_L \approx 0.6$ as opposed to $C_L \approx 0.2$ as in the current study. This further motivates the current investigation into the cause of breaks in the stability curves of thin wings at low Reynolds numbers specifically at low lift coefficients. Although the breaks in the stability curve at $C_L \approx 0.2$ and $C_L \approx 0.5$ are explicitly identified here for the tapered wings shown, they occur for all tested wings at approximately the same lift coefficient. As is shown and explained in later sections of this work, what differs between wings is not the lift coefficient of these breaks but the change in C_{l_β}/C_L associated with each break. We will show this to be a direct function of the sweep angle of the wing.

To investigate the observed breaks in the stability curves at $C_L \approx 0.2$ and $C_L \approx 0.5$ of Fig. 6 as well as additional breaks that occur at higher lift coefficients, surface oil-flow visualizations were conducted on the forward- and backward-swept wings at both zero and nonzero sideslip angles at select angles of attack. For surface oil-flow visualizations, a replica sting balance was mounted to the pressure side of the wing, and tape was used to cover mounting holes on the suction surface to leave a clean top surface for pigment transport. The oil mixture consisted of paraffin oil and commercially available fluorescent pigment (Art 'N Glow pigment powder, particle size 30–50 μm). The mixture was applied to the wing with a brush, with the wing mounted to the positioning system at zero pitch angle. Brush strokes were made perpendicular to the leading edge of the forward-swept wing and perpendicular to the left leading edge of the backward-swept wing. After coating the wing, the wing was commanded to the desired pitch angle via the positioning system, and the tunnel velocity was rapidly ramped up to the prescribed freestream velocity. After > 5 min of run time, the pigment was charged with a UV flashlight, and the wing was imaged at inclination with a 12 megapixel camera with the wind tunnel still running.

For the forward-swept wing, surface oil-flow visualizations were supplemented with streamwise particle image velocimetry (PIV) measurements taken at the midspan of the wing at zero sideslip at select angles of attack. The PIV measurements were taken using the same wing model and mounting rig and at the same flow speed as the stability derivative measurements. For the current measurements, 386 images were taken at 100 Hz, which corresponds to 3.86 s of sampling time. Spanwise vorticity was computed from the instantaneous velocity fields using the local circulation method [43].

The stability curve of the forward-swept wing is shown in Fig. 7. Here, $-C_{l_\beta}$ is plotted as a function of C_L until $C_{L_{\max}}$. At select lift coefficients, spanwise vorticity contours and time averaged velocity fields, displaying every other measured velocity vector, are inset. Included below the stability curve are surface oil-flow visualization images taken at the labeled lift coefficients. The top and bottom rows correspond to surface-oil patterns obtained for the wing at $\beta = 0$ deg and $\beta = 10$ deg, respectively.

At low lift coefficients in the range $0 < C_L < 0.2$, the flow remains laminar over the chord of the wing and is attached in the averaged sense. Here, vorticity is confined to thin boundary layers, which are not resolved by the PIV measurements taken at lift coefficients marked by A. The absence of surface-oil patterns over the wing at A further corroborates this attached-flow condition. The slope $-C_{l_\beta}/C_L$ is nearly zero for this wing, which is in stark contrast to the rectangular and backward-swept wing at this lift coefficient range (recall Fig. 6).

At lift coefficients in the range $0.2 < C_L < 0.5$, a distinct break change in slope $-C_{l_\beta}/C_L$ occurs. In this lift coefficient range, $-C_{l_\beta}$ increases with lift coefficient at a faster rate than at lower lift coefficients. PIV measurements and surface oil visualizations suggest that the change in stability is attributed to the initial existence of separated and subsequently reattached leading-edge flow. PIV measurements taken in this range, specifically at B, display strong concentrated vorticity near the leading-edge of the wing and a thick diffusive boundary layer aft, collectively indicating transitional flow in the form of a separation bubble. Surface flow patterns corroborate the occurrence of a separation bubble because, at B, a clear separation line (as marked by the yellow line) is observed on both the wing at zero and nonzero sideslip angle. The carrier fluid, driven by pressure, gravitational, and shear forces, puddles above this line as it cannot penetrate the reverse flow associated with the separation bubble. The effect of sideslip is to break the spanwise symmetry of the bubble across the span of the wing.

At higher lift coefficients in the range $0.5 < C_L < 0.7$, the slope $-C_{l_\beta}/C_L$ increases yet again for this wing. Analysis of PIV measurements and surface oil visualizations suggest that the cause of increased lateral stability in this regime is associated with the spanwise variation of separated flow across the wing. At the lift coefficients marked by B, vorticity measurements stemming from the leading-edge takes the form of a "free" shear layer in the sense that it is lifted off the wing and more nearly aligned with the freestream velocity vector. Analysis of movies of the instantaneous vorticity fields display highly unsteady and intermittent flow reattachment associated with transitional vortex shedding at this lift coefficient. We suspect that the downwash over the wing is insufficient to stably reattach the leading-edge flow at the midspan of the wing. Surface-oil patterns depict significant spanwise variation across the wing. The lack of downstream shear and the unsteadiness of flow reattachment at the midspan results in the puddling of carrier fluid (dark regions observed at C) centered on the wing. At spanwise locations outboard of the midspan, the surface-oil patterns transition into a single distinct separation line, reminiscent of that observed on the wing at the lower lift coefficient, marked by B; this pattern was attributed to the separation bubble. Surface-oil patterns of the wing in sideslip depict a leeward shift of those observed on the wing at zero sideslip. These patterns in sideslip suggest that the leeward portion of the wing experiences more advanced stages of leading-edge flow separation than the windward wing. This asymmetry in leading-edge flow reattachment across the span of the wing would contribute to a negative roll moment at this positive sideslip angle, which is stabilizing by the definition of lateral stability (i.e., $-C_{l_\beta} > 0$).

At lift coefficients $C_L > 0.7$, $-C_{l_\beta}$ now decreases with increasing lift until $C_L \approx 0.98$. PIV measurements and surface oil visualizations suggest that this trend is connected to the more stable reattachment of leading-edge flow at the midspan and the subsequent formation of a leading-edge separation region on the wing at these lift coefficients.

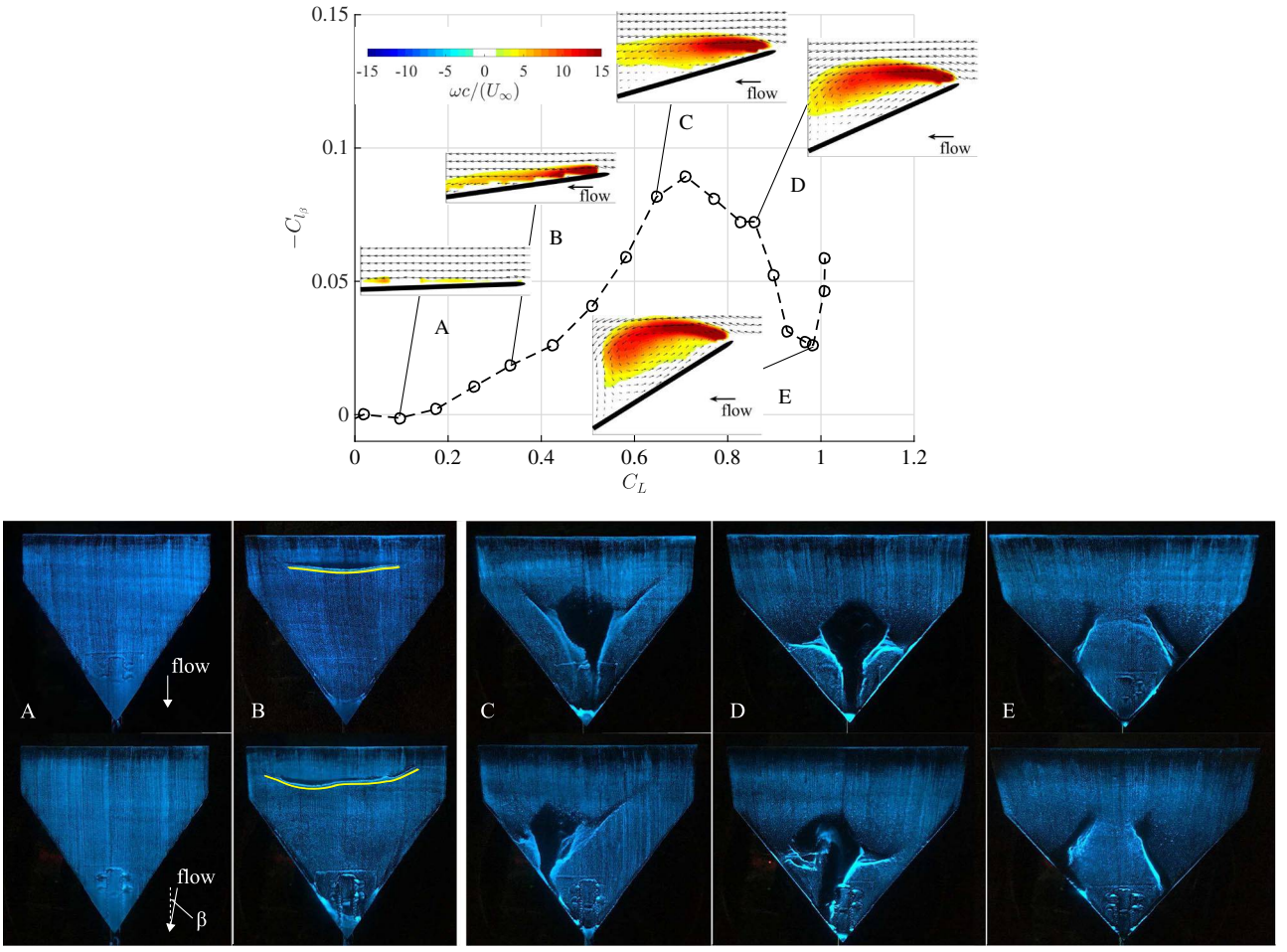

Fig. 7 Lateral stability curve and corresponding flow visualizations for the forward swept wing ($\mathcal{AR} = 1.6, \lambda = 0.25, \Lambda = -20.6$ deg) at $\beta = 0$ deg and $\beta = 10$ deg.

From the flow measurements in Fig. 7 at D and E, the leading-edge shear layer curves back toward the wing, and strong reverse flow is evident near the suction surface of the wing. At E, movies of instantaneous measurements depict the recirculation of leading-edge vorticity above the wing as opposed to the downstream shedding of leading-edge vorticity measured to occur at lower lift coefficients. The more stable reattachment of leading-edge flow forms a leading-edge separation region and establishes an effective bound circulation [27] around the wing, composed of the bound circulation of the wing itself and the circulation of the leading-edge separation region, which sustains the lift-generating ability of the wing to higher angles of attack. The oil-surface flow visualizations conducted on the wing, specifically at E, depict what the authors believe to be the surface footprint of the leading-edge separation region. This structure is observed to shift toward the leeward wing. Similar to that measured to occur on rectangular wings [6], a leeward shifting of the leading-edge separation region would tend to increase lift on the leeward wing favoring a roll moment that is destabilizing in terms of C_{l_β} (i.e., a positive roll moment at a positive sideslip angle). This is consistent with the measured reduction in lateral stability on this wing from $0.7 < C_L < 0.98$, suggesting that the formation of a leading-edge separation region on the wing in this lift coefficient range is a plausible cause of this trend. At $C_L > 0.98$, the magnitude of $-C_{l_\beta}$ is measured to recover just before $C_{L_{\max}}$. Additional measurements are needed in this regime to resolve this stability trend.

Figure 8 plots the stability curve of the backward-swept wing up until $C_{L_{\max}}$. Surface oil-flow patterns of the wing both at zero and nonzero sideslip are also included. The top and bottom row

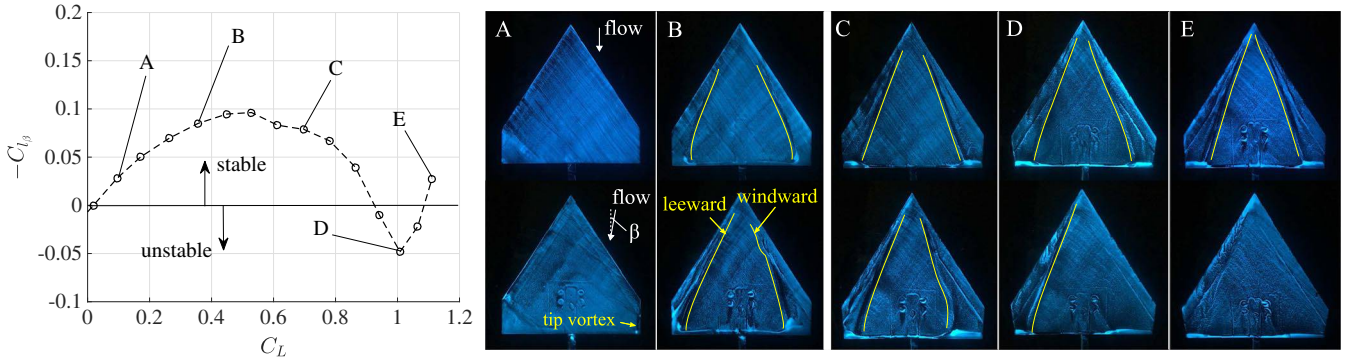

Fig. 8 Lateral stability curve and corresponding surface-oil visualizations for the backward swept wing ($\mathcal{AR} = 1.6, \lambda = 0.25, \Lambda = 48.4$ deg) at $\beta = 0$ deg and $\beta = 10$ deg.

correspond to $\beta = 0$ deg and $\beta = 10$ deg, respectively. The moderate quarter-chord sweep angle (48.4 deg) and strong tapering of this wing make it geometrically similar to a nonslender delta wing. Therefore, it is instructive to briefly recall the key features of the flow over nonslender delta wings. Gursul et al. [44] provide a great review of such literature. For sufficiently thin wings, boundary-layer separation occurs at the leading edges of the wing, resulting in the formation of three-dimensional shear layers. Unlike slender delta wings, where the shear layers roll into a pair of counter-rotating primary vortices, the shear layers on nonslender delta wings form elongated regions of separated flow. Each separation region can consist of a primary vortex or a primary and secondary vortex, with the latter dual-vortex structure being formed due to the interaction of secondary flow and the primary shear layer. At the current Reynolds number of 75,000, the separation region is likely to be transitional.

With this framework of nonslender vortical flows in mind, we turn to analyzing the surface-oil patterns over this wing (Fig. 8). For visual assistance, secondary separation lines are marked by a yellow line; this line is placed immediately inboard of the actual separation line. Tertiary separation lines can also be distinguished outboard of the secondary separation line at certain lift coefficients. Primary attachment lines cannot be distinguished in the surface-oil visualizations. Nevertheless, it will be shown that critical changes in the lateral stability curve of this wing can be explained by analyzing asymmetries in the existence and/or distortion of the secondary separation line. As such, analysis of other separation/attachment lines is considered outside the scope of the current work.

Turning attention to Fig. 8, at low lift coefficients $0 < C_L < 0.2$, $-C_{l_\beta}$ increases with lift coefficient for this wing. The increase in lateral stability with lift coefficient in this range is in stark contrast to the previously discussed stability curve of the forward-swept wing (recall Fig. 7). Surface-oil patterns on the current wing at zero sideslip at the lift coefficient marked by A suggest that the flow remains attached to the wing due to the absence of any distinct surface pattern on the wing. However, for the corresponding sideslip case, a distinct separation line is evinced near the windward wing tip of the wing, indicating separated flow over the wing in the form of a wing-tip vortex. The orientation of the separation line suggests that this tip vortex convects over the wing in the direction of the freestream, similar to what was observed for the wings in Fig. 3 via smoke-wire visualizations. In this lift coefficient range, we expect a modified Queijo theory [Eq. (2)] to be able to accurately capture the slope $-C_{l_\beta}/C_L$ so long as the tip vortex effect is addressed.

At higher lift coefficients in the range $0.2 < C_L < 0.5$, the slope $-C_{l_\beta}/C_L$ gradually decreases. Surface-oil patterns taken at B display two distinct secondary separation lines on each semispan of the wing, suggesting the separation, reattachment, and subsequent secondary separation of leading-edge flow. Based on this observation, we attribute the initial change in slope $-C_{l_\beta}/C_L$ in this lift coefficient range to the occurrence of separated leading-edge flow over the wing. Unlike the forward-swept wing, which experiences an increase in $-C_{l_\beta}/C_L$ due to the initial existence of flow reattachment, the backward-swept wing experiences decrease in $-C_{l_\beta}/C_L$. The surface flow patterns at B on this wing in sideslip reveal a break in symmetry of the separation lines on the wing where the secondary separation lines on both the leeward and windward portions of the wing shift in the direction of the crossflow introduced over the wing. The separation line previously attributed to the tip vortex can no longer be made out at this lift coefficient.

At $0.5 < C_L < 0.7$, the slope $-C_{l_\beta}/C_L$ is now negative, and the magnitude of C_{l_β}, or the lateral static stability of the wing, begins to gradually decrease with increasing lift coefficient. Surface-oil patterns at C for the wing in sideslip display strong asymmetry in the location of the secondary separation line on the wing where the windward secondary separation line is located more inboard on the wing than at the lower lift coefficient marked by B most notably near the aft portion of the wing. From $0.8 < C_L < 1$, C_{l_β} decreases with lift at a much faster rate. In this lift coefficient range, C_{l_β} actually becomes negative starting at $C_L \approx 0.9$, indicating that the wing is statically unstable in roll at these lift coefficients. Surface-oil patterns at D ($C_L \approx 1$) display asymmetry in the existence of the secondary separation line on the wing. Specifically, the separation line on the windward wing has vanished, suggesting that the windward wing has stalled. The presumed asymmetry in reattached/stalled flow on the leeward and windward wing, respectively, would contribute to a reduction in lateral static stability $-C_{l_\beta}$ as well as a reduction in lift. Both of these trends are observed to occur in load measurements, with the former trend being reflected in the stability curve in Fig. 8 and the latter trend being reflected in lift measurements presented in Fig. 5. Therefore, the stability reversal observed for this wing is likely caused by asymmetric wing stall. At higher lift coefficients short of lift stall, $-C_{l_\beta}$ begins to increase with increasing lift coefficient as the windward wing progresses toward stall which reduces the asymmetry in flow conditions over the windward and leeward portions of the wing.

From this characterization of the lateral stability curves of two representative wings, we have observed that the existence of separated but reattached leading-edge flow contributes to nonlinear trends in the lateral stability curves at lift coefficients as low as $C_L \approx 0.2$. For initial lift coefficients greater than $C_L \approx 0.2$, the effects of reattached flow on the lateral static stability of the wing could be stabilizing, such as the case for the unswept wing, or destabilizing, such as the case for the swept wing. Because accurate prediction of changes in lateral stability with changing lift is necessary to predict looming changes in an aircraft's roll response at different flight conditions, one cannot ignore the effects of flow reattachment on stability trends. In a later section, we will attempt to model the early developmental stages of leading-edge flow reattachment, specifically $C_L < 0.5$, and its effects on lateral stability.

IV. Modeling of C_{l_β} for Thin Wings at Low Reynolds Numbers

In this section, we propose a series of modifications to the Queijo model to improve the prediction of the lateral static stability derivative C_{l_β} of thin low-$\mathcal{R}$ wings at low Reynolds numbers. We limit the scope of this work to predicting C_{l_β} at both low lift coefficients, where separated flow is limited to the wing tips and moderate lift coefficients involving the initial existence of separated but reattached leading-edge flow. The corresponding lift coefficient ranges are $C_L < 0.2$ and $0.2 < C_L < 0.5$, respectively, for the tested wings. These two regimes are depicted in the surface oil-flow visualizations of the moderately tapered swept wing in Fig. 9, where the secondary separation lines are indicated with solid lines, and in the previously presented surface oil visualizations in Figs. 8 and 7 at lift coefficients marked by A and B.

A. Accounting for Tip Vortex Roll-Up

We seek a new vortex element to represent the wing in sideslip that accounts for the roll-up of the tip vortex over the windward portion of the wing (recall Figs. 3 and 9). The separation lines associated with the windward tip vortex in Fig. 9 take on an angle δ (relative to the chord of the wing) slightly less than β at $\alpha = 2$ deg and nearly equivalent to β at $\alpha = 8$ deg, with the latter point suggesting that the windward tip vortex is oriented in the direction of the freestream velocity vector. The orientation of the tip vortex in sideslip will

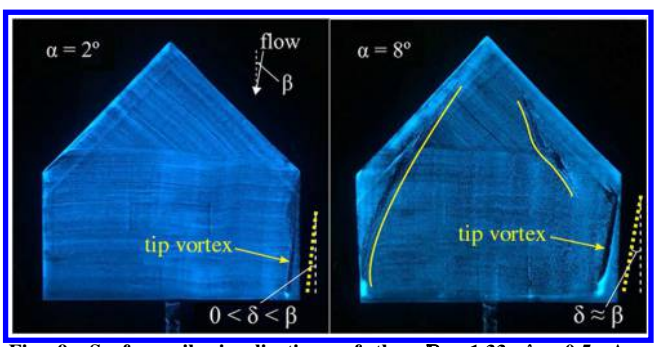

Fig. 9 Surface oil visualizations of the $\mathcal{R} = 1.33$, $\lambda = 0.5$, $\Lambda = 36.9$ deg wing at $\beta = 10$ deg. Angle of attack is as marked.

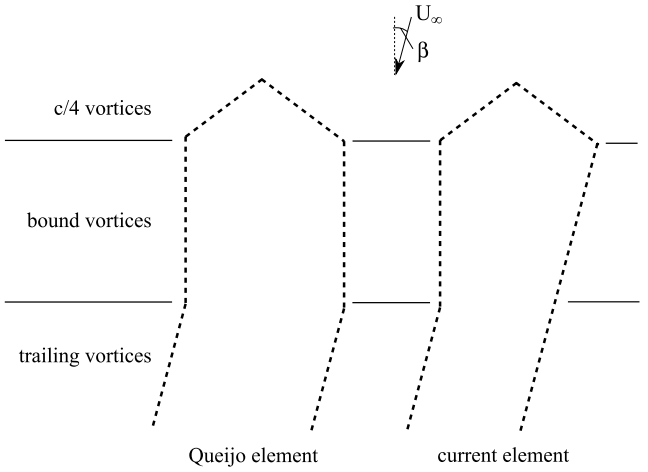

Fig. 10 Comparison between the vortex elements of Queijo [3] and the current work.

modify the flow tangency condition on the wing such that the flow near the windward wing tip will be directed approximately in the direction of the freestream velocity as opposed to the chordwise direction. To accommodate this feature for modeling purposes, the windward bound vortex on the proposed element is now oriented parallel to the freestream velocity vector.

Figure 10 depicts the new vortex element, placed next to the vortex element of Queijo [3]. By reorienting the windward bound vortex in the direction of the freestream velocity, this vortex segment now behaves like a "free vortex" in the sense that it does not contribute to a lift force in sideslip. As such, the windward bound vortex no longer contributes to the C_{l_β} of the wing. Clearly, this small modification to the windward bound vortex element would only effect C_{l_β} prediction of wings for which a substantial portion of the increment in lift due to sideslip stems from chordwise bound vortices (i.e., low-aspect-ratio untapered wings). This will be shown to be the case.

To demonstrate the improvement in stability derivative prediction using this new element, we derive an equation for the stability coupling ratio C_{l_β}/C_L using a single vortex element and compare its predictive ability against experimental stability derivative measurements and the theory of Queijo [Eq. (2)]. The derivation of C_{l_β}/C_L is described next.

A linearly tapered swept wing, defined by its quarter-chord sweep angle Λ, taper ratio $\lambda \equiv c_t/c$, and aspect ratio $\mathcal{R} \equiv b^2/S$, is replaced with a single skewed vortex element of circulation Γ, as shown in Fig. 11. The total lift of the wing is determined by summing the lift contribution of each of the vortex segments. The lift per unit length of a vortex element of constant circulation in a fluid of density ρ is given

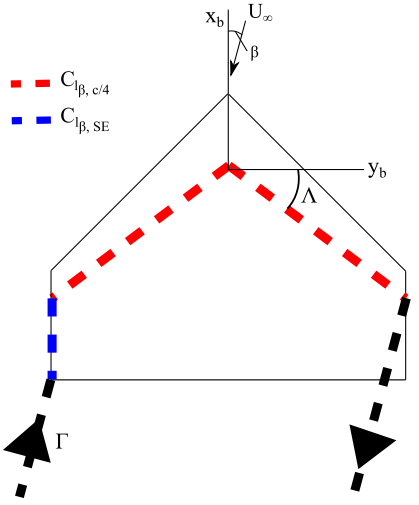

Fig. 11 Vortex model for the wing in sideslip.

by the Kutta–Joukowski equation $dL = \rho U_\perp \Gamma d\delta$, where $U_\perp$ is the component of the velocity that is perpendicular to the vortex axis. The equation reduces to the following formula for vortex segments of finite length δ and constant Γ:

$$L = \rho U_\perp \Gamma \delta$$

For each semispan, the $c/4$ vortices experience a lift force $L_{c/4}$ equal to

$$L_{c/4} = \rho U_\infty \cos(\Lambda \pm \beta)\Gamma\left(\frac{b/2}{\cos(\Lambda)}\right) \tag{4}$$

where $(b/2/\cos(\Lambda))$ is the length of the $c/4$ vortex segment on one semispan. The $\pm$ in the preceding equation corresponds to the left and right semispan, respectively. The force due to sideslip for the bound vortex on the leeward wing's side edge, or L_{SE}, is given by

$$L_{\mathrm{SE}} = -\rho U_\infty \sin(\beta)\Gamma\left(\frac{3(c_r\lambda)}{4}\right)$$

where the length of the vortex segment is $3(c_r\lambda)/4$. Note that the windward bound vortex and trailing-edge vortex do not contribute to lift because these vortices are oriented parallel to the freestream velocity. Expanding the trigonometric term in Eq. (4), employing the small sideslip assumption [$\cos(\beta) \approx 1$ and $\sin(\beta) \approx \beta$], then taking the partial derivative of the lift force with respect to sideslip, we obtain the increment in lift due to sideslip for these vortex segments as

$$\begin{aligned}(L_\beta)_{c/4} &= \rho U_\infty(\cos(\Lambda) \mp \beta \sin(\Lambda))\Gamma\left(\frac{b/2}{\cos(\Lambda)}\right)\\ &= \mp\rho U_\infty \tan(\Lambda)\Gamma(b/2)\end{aligned}$$

for the $c/4$ vortex, where $\mp$ corresponds to the vortices on the left and right semispan, respectively, and

$$(L_\beta)_{\mathrm{SE}} = -\rho U_\infty \beta \Gamma\left(\frac{3(c_r\lambda)}{4}\right)$$

for the side-edge vortex. We note that, for the rectangular wing with its unswept leading edge (i.e., $\Lambda = 0$ deg), the side-edge vortex is the sole contributor to an increment in lift due to sideslip. Nondimensionalizing by standard aerodynamic definitions $C_L = (2L/\rho U_\infty^2 S)$, we obtain

$$(C_{L_\beta})_{c/4} = \mp\frac{\Gamma}{U_\infty S}\tan(\Lambda)(b/2) \tag{5}$$

and

$$(C_{L_\beta})_{\mathrm{SE}} = -\frac{\Gamma}{U_\infty S}\left(\frac{3(c_r\lambda)}{4}\right) \tag{6}$$

We are left to determine a relation for the characteristic circulation Γ of the vortex element. This circulation should be equivalent to that which is required to sustain the total lift generated by the wing. For simplification, we assume that the total lift of the wing and corresponding characteristic circulation remains unchanged at small sideslip. This assumption is the same employed by Weissinger and Queijo and is further corroborated by analyzing the lift curves shown in Fig. 5, which show that the lift generated before stall remains unchanged at small sideslip $|\beta| \leq 10$ deg. This feature is representative of all wings tested in this study.

Employing this assumption, $\Gamma = \Gamma_{\beta=0\ \mathrm{deg}}$, where $\Gamma_{\beta=0\ \mathrm{deg}}$ is the characteristic circulation of the wing at zero sideslip. At zero sideslip, the lift generated by the wing stems solely from the $c/4$ vortices because the bound vortices and trailing vortices remain parallel to the freestream. The total lift of the wing at zero sideslip $\Gamma_{\beta=0\ \mathrm{deg}}$ is therefore the summation of lift contributions of the $c/4$ vortices and is given by

$$L_{\beta=0\ \deg} = \rho U_\infty \Gamma_{\beta=0\ \deg} b$$

Upon nondimensionalization, and rearrangement, an expression for the characteristic circulation Γ in terms of $C_{L_{\beta=0\ \deg}}$ is obtained as

$$\Gamma = \frac{C_{L_{\beta=0\ \deg}}}{b} U_\infty S \tag{7}$$

Here, we have employed the approximation $\Gamma = \Gamma_{\beta=0\ \deg}$. Incorporating Eq. (7) into the lift derivatives due to sideslip [Eqs. (5) and (6)] results in

$$(C_{L_\beta})_{c/4} = \mp\frac{1}{2} C_{L_{\beta=0\ \deg}} \tan(\Lambda) \tag{8}$$

and

$$(C_{L_\beta})_{SE} = -\frac{3}{4} C_{L_{\beta=0\ \deg}} \left(\frac{\lambda}{\mathcal{R}(1+\lambda)}\right) \tag{9}$$

Note that our interest is in the change in roll moment due to sideslip. Therefore, our task now is to determine the proper moment arm for which the various loads act. The moment arm for the side-edge vortex is trivial and is taken as the wing's semispan $b/2$. The moment arm due to the $c/4$ vortex segments is less trivial. For now, let us denote the moment arm for the $c/4$ vortices as $\bar{y}$. We will revisit this shortly.

The roll moment due to sideslip or the lateral static stability derivative C_{l_β} is given in terms of the increment in lift due to sideslip of the $c/4$ and side-vortex elements as

$$C_{l_\beta} = \frac{1}{b}\left[-2|(C_{L_\beta})_{c/4}|\bar{y} + (C_{L_\beta})_{\mathrm{SE}} \frac{b}{2}\right] \tag{10}$$

Note that the $1/b$ term arises from the nondimensionalization of roll moment, which is $C_l = (2l/\rho U_\infty^2 S b)$. The absolute value is used due to the reflective symmetry of $(C_{L_\beta})_{c/4}$, where a positive increment in lift due to sideslip occurs on the windward wing, and negative increment in lift due to sideslip occurs on the leeward wing, resulting in a roll moment about the midspan of the wing that is in the same $(-x_b)$ direction.

In the distributed vortex model of Queijo, the moment arm of the $c/4$ vortex was denoted as $\bar{y}$ and was referred to as the centroid of angle-of-attack loading. Recovery of $\bar{y}$ requires knowledge of the distribution of the additional load on the wing due to angle of attack changes. With knowledge of this load distribution, one can compute the bending or "roll" moment increment distribution and obtain the total root bending moment upon integration of the bending moment distribution across the span. One can then compute the spanwise center of pressure ($\bar{y}$) through simple statics using knowledge of the total load on the wing. Values of $\bar{y}^*$, where the asterisk refers to nondimensionalization by the wing semispan $b/2$, were calculated for a wide range of wings by various authors [45]. Using these data, Queijo [46] compiled look-up tables that tabulated $\bar{y}^*$ as a function of sweep, aspect ratio, and taper ratio. Upon analyzing these look-up tables of $\bar{y}^*$, the spanwise center of pressure $\bar{y}^*$ varies only slightly within the range 0.4–0.45 for low-aspect-ratio wings of $\mathcal{R} \approx 1.5$ having sweep angles ranging from $\Lambda = -45$ to 60 deg and taper ratios ranging from $\lambda = 0.25$–1. As an approximation, a $\bar{y}^*$ value of 0.425 is used both for the current theory and that of Queijo when comparing to experimental measurements of the wings in this study.

Combining Eqs. (8) and (9) with Eq. (10) and employing the definition of aspect ratio for linearly tapered wings, $\mathcal{R} \equiv b^2/S = (2b/c_r(1+\lambda))$, we obtain an expression for the slope C_{l_β}/C_L as

$$\frac{C_{l_\beta}}{C_L} = \left(\frac{C_{l_\beta}}{C_L}\right)_{c/4} + \left(\frac{C_{l_\beta}}{C_L}\right)_{SE} = -\left[\frac{1}{2}\tan(\Lambda)\bar{y}^* + \frac{3}{4}\left(\frac{\lambda}{\mathcal{R}(1+\lambda)}\right)\right] \tag{11}$$

Here, the asterisk implies the following nondimensionalization: $\bar{y}^* = (\bar{y}/b/2)$. Note that we have dropped the subscript in $C_{L_{\beta=0\ \deg}}$.

Notice that, if we did not account for the tip vortex effect, the side-edge vortex contribution or $(C_{l_\beta}/C_L)_{\mathrm{SE}}$ would be twice that in Eq. (11). Therefore, the effect of the tip vortex is to reduce the magnitude of $-C_{l_\beta}/C_L$ over the same wing for which the tip vortex roll-up did not occur. In this sense, the roll-up of the tip vortex over the wing is a destabilizing feature in terms of the lateral static stability of a wing.

Figure 12 compares the current theory of Eq. (11) to experimental measurements for the limiting case of the rectangular wing ($\Lambda = 0$ deg, $\lambda = 1$). Because $\Lambda = 0$ deg, the lateral static stability of the rectangular wing stems solely from the chordwise oriented bound vortex or $(C_{l_\beta}/C_L)_{\mathrm{SE}}$; therefore, Eq. (11) reduces to $C_{l_\beta}/C_L = -(3/8)(1/\mathcal{R})$. Also included is the theory of Queijo [Eq. (2)], which for the rectangular wing is equivalent to that of Weissinger [Eq. (1)], with $\kappa = 1.5$. Figure 12a plots the stability ratio C_{l_β}/C_L directly as a function of aspect ratio for the rectangular wings. The current theory is more accurate than the theory of Queijo for the wings of the current study because it accounts for the effect of the tip vortex on C_{l_β}. Figure 12b plots the product $-C_{l_\beta}\mathcal{R}$ as a function of lift coefficient. When plotted this way, the stability curves of the various aspect ratio wings collapse to a single line, which is accurately predicted by the current theory. Equation (2) does not predict the collapse due to the additional term of 0.05 in the equation. Note that this value is placed by Queijo and Weissinger to account for the change in circulation due to sideslip associated with the occurrence of bent trailing vortex sheet in sideslip. We do not incorporate this effect because the force measurements indicate that the total lift of the wing remains unchanged at small sideslip angles. It is likely that the change in circulation with sideslip associated with the bent trailing vortex wake is attenuated by the sharp edge effects of the thin wings used in this study. Recall that the wings that were used for validation by Queijo [3] were generally thick, $t/c = 12\%$. Therefore, the collapse of the stability curves may simply be a feature of thin wings and not necessarily associated with Reynolds number effects. More work is required to further investigate this feature.

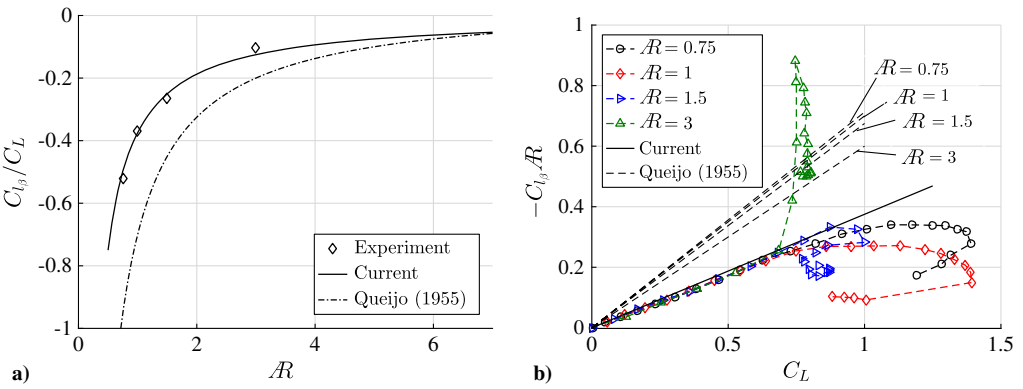

Fig. 12 Representations of the lateral static stability derivative as a function of lift coefficient and wing $-C_{l_\beta}\mathcal{R}$ for rectangular wings.

Let us take a moment to analyze the physical ramifications of the scaling of the roll moment coefficient C_l for unswept wings. From classical aircraft mechanics, it is customary to express the nondimensional roll moment as $C_l = (l/qSb)$ using the span of the wing b as the reference length,where q is the dynamic pressure. In the context of unswept wings, a more physical length scale should be the chord of the wing. This stems from the fact that the magnitude of roll moment due to sideslip (i.e., crossflow over the wing) is solely dependent on the lift of chordwise bound vortices on unswept wings. To exemplify this, consider the static roll moment coefficient of a rectangular wing in symmetric flight. To first order, C_l can be expressed as

$$C_l = C_{l_\beta}\beta$$

Combining with Eq. (11) for rectangular wings ($\Lambda = 0$ deg, $\lambda = 1$), C_l becomes

$$C_l = \frac{3}{8}\frac{C_L}{\mathcal{R}}\beta$$

Multiplying both sides by $\mathcal{R}$, one obtains

$$C_l\mathcal{R} = \frac{3}{8}C_L\beta \tag{12}$$

Analyzing the left-hand side of the Eq. (12), we can define a new nondimensional coefficient of roll moment as C_l^* as

$$C_l^* = C_l\mathcal{R} = \frac{l}{qSb}\mathcal{R}$$

where the term l/qSb stems from the classical nondimensionalization of roll moment l. Employing the definition of $\mathcal{R}$ for rectangular wings, $\mathcal{R} = b/c$, C_l^* becomes

$$C_l^* = \frac{l}{qSc} \tag{13}$$

Equation (13) depicts a more physical nondimensionalization of roll moment for rectangular wings, which uses the chord of the wing as reference length instead of the span of the wing.

Turning our attention back to Fig. 12b, the linearity and scaling of C_{l_β} is lost for $C_L > 0.7$. For the $\mathcal{R} = 3$ wing, this corresponds to lift stall. For the $\mathcal{R} < 1.5$ wings, this corresponds to the formation of a recirculatory leading-edge separation region. The flow physics in this nonlinear regime was studied extensively by the authors in [6]. Note that separated leading-edge flow still exists over the wing at lower lift coefficients $C_L < 0.7$; however, the linearity between C_{l_β} and C_L is still maintained. As was shown in Sec. III, this is not the case for swept wings where this linearity is lost at $C_L \approx 0.2$ due to separated leading-edge flow. This leaves the current linear model for C_{l_β} of limited use for swept wings. We now seek to accommodate the physics of the separation bubble into our model.

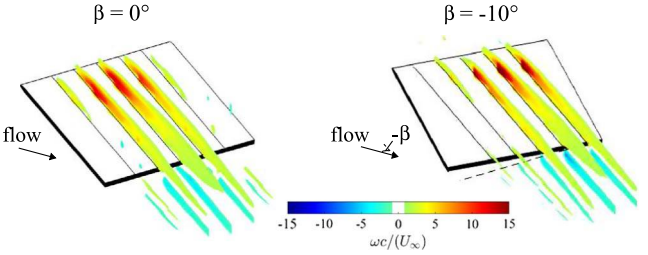

Fig. 13 Cross-stream vorticity contours obtained via stereo-digital particle image velocimetry at several streamwise measurement planes spanning the $\mathcal{R} = 1$ wing at both zero and nonzero sideslip. Adapted from [6].

on an $\mathcal{R} = 1$ rectangular wing at $\alpha = 10$ deg. These data were adapted from Linehan and Mohseni [6]. The leading-edge vorticity shifts in the direction of the crossflow while remaining attached or aligned with the chord of the wing. In this sense, although the vorticity associated with the separated flow will continue to contribute to the total lift of the wing (due to its inclination relative to the freestream velocity), it will not contribute to an increment in lift due to sideslip, or L_β, as it yields to the crossflow. Therefore, the flow associated with the leading edge of the wing should not contribute to C_{l_β}/C_L of the wing in this lift coefficient range. Similar features associated with the shifting of leading-edge flow in the direction of the crossflow velocity are expected to occur for the swept wings. This is believed because the surface oil visualizations conducted on swept wings in sideslip in this lift coefficient range depict a leeward shift in the separation lines on the wing. A modification to the current model that accounts for these physics should extend the predictive ability of the model to higher lift coefficients for wings tested in this study.

To account for this in the framework of the current model, the sideslipped wing at $0.2 < C_L < 0.5$ is modeled as shown in Fig. 14. Specifically, the $c/4$ vortex is oriented such that it no longer generates an increment in lift due to sideslip, i.e., $(L_\beta)_{c/4} = 0$, specifically for small sideslip angles. This mirrors the fact that the vorticity associated with separated flow at this lift coefficient would not contribute to L_β as it yields to the crossflow. Although the $c/4$ vortex does not contribute to L_β, it still contributes to the total lift of the wing. In fact, the total lift of the vortex system remains unchanged from that which would be generated by the vortex arrangement used for lift coefficients in the range $0 < C_L < 0.2$.

Based on the above arguments, the only contributor to C_{l_β}/C_L at lift coefficients in the range $0.2 < C_L < 0.5$, is the leeward side-edge vortex. The equation for C_{l_β}/C_L becomes piecewise-linear as

$$\frac{C_{l_\beta}}{C_L} = -\begin{cases} \frac{1}{2}\tan(\Lambda)\bar{y}^* + \frac{3}{4}\left(\frac{\lambda}{\mathcal{R}(1+\lambda)}\right) & 0 < C_L < 0.2, \quad \text{attached flow} \\ \frac{3}{4}\left(\frac{\lambda}{\mathcal{R}(1+\lambda)}\right) & 0.2 < C_L < 0.5, \quad \text{leading-edge flow reattachment} \end{cases} \tag{14}$$

B. Accounting for the Early Stages of Leading-Edge Flow Reattachment

To assist in explaining the impact of separated leading-edge flow at low lift coefficients on lateral stability, Fig. 13 displays cross-stream vorticity contours at $\beta = 0$ deg and $\beta = -10$ deg to accommodate the different flow physics at lift coefficients involving attached leading-edge flow and lift coefficients involving initial lift coefficients involving leading-edge flow reattachment.

Equation (14) states that, at low angles of attack, the slope C_{l_β}/C_L will be dictated by the sweep angle, aspect ratio, and taper ratio,

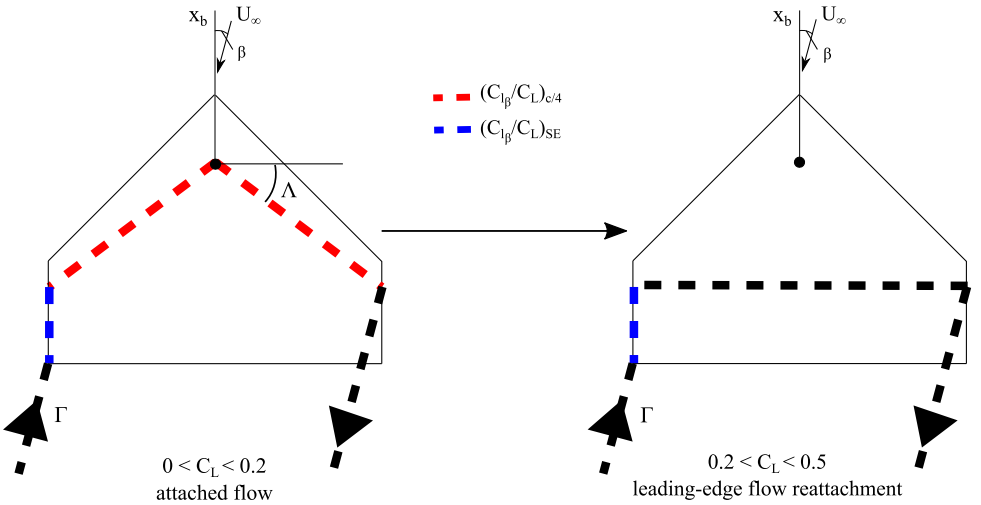

Fig. 14 Vortex representation for the wing in sideslip at lift coefficients involving attached flow, $0 < C_L < 0.2$, and lift coefficients involving separated but reattached flow, $0.2 < C_L < 0.5$.

whereas at initial angles of attack involving the formation of a separation bubble, the slope C_{l_β}/C_L will be solely dictated by the wing aspect ratio and taper ratio. In this representation, the effect of the separation bubble is stabilizing for the forward-swept wing as the slope $-C_{l_\beta}/C_L$ increases in magnitude in this lift coefficient range over that which occurs at the lower lift coefficient range. For the backward-swept wing, flow separation is destabilizing as $-C_{l_\beta}/C_L$ decreases in magnitude. The magnitude of the change in slope $-C_{l_\beta}/C_L$ in this regime is proportional to the sweep of the wing. For the unswept wing, the separation bubble has no effect on the lateral static stability trends of the wing.

Figure 15 plots C_{l_β} versus C_L for the various swept wings tested. Columns designate wings of constant aspect ratio and taper ratio as noted. Within each column, the sweep angle of the wing increases with increasing row. For each wing, C_{l_β} is plotted up until $C_{L_{\max}}$. Also included are theoretical predictions of the current theory [Eq. (14)] and that of Queijo [Eq. (2)]. The current theory more accurately predicts C_{l_β} over the theory of Queijo for all wings in this study. This consists of both low lift coefficients $C_L < 0.2$, for which the leading-edge flow is attached, and initial lift coefficients involving separated but reattached flow, $0.2 < C_L < 0.5$.

The core rationale for the improvement in stability derivative prediction is the acknowledgment of separated flow over the wing. At low lift coefficients, the flow separates over the windward portion of the sideslipped wing in the form of a tip vortex oriented in the direction of the freestream (recall Figs. 3 and 9). We accommodate this feature by reorienting the bound vortex on the windward wing to satisfy the flow tangency condition imposed by the tip vortex. In doing so, the stability contribution of the bound vortices of our model is always less than that of the Queijo model. We believe the Queijo model to be valid for lifting surfaces for which tip vortex roll-up occurs in the wake, likely thick wings at high Reynolds numbers. For the highly swept wing with the largest aspect ratio (Fig. 15g), the distinction between the two theories at low lift coefficients is very small. This is because, as the aspect ratio and sweep angle of the wing increase, the chordwise bound vortices contribute less to the stability of the wing. Therefore, the current vortex model does not have a significant impact on the prediction of stability derivatives of high-$\mathcal{AR}$ swept wings at lift coefficients involving attached leading-edge flow. The current theory, specifically at low lift coefficients, is mainly important for the design of thin low-$\mathcal{AR}$ wings at low Reynolds numbers.

At higher lift coefficients in the range $0.2 < C_L < 0.5$, flow separates near the leading-edge of the wing and subsequently reattaches to the wing. Depending on the sweep angle of the wing, the occurrence of reattached leading-edge flow can further increase the slope $-C_{l_\beta}/C_L$ or decrease it. The current theory captures this effect. For the forward-swept wing (Fig. 15a), the effect of leading-edge flow reattachment in this lift coefficient range is to increase the magnitude of the slope $-C_{l_\beta}/C_L$. In contrast, the backward-swept wing (Fig. 15g) experiences a decrease in the magnitude of $-C_{l_\beta}/C_L$ due to leading-edge flow reattachment. Moreover, for wings of low sweep angle and low $\mathcal{AR}$ (Fig. 15f), the change in $-C_{l_\beta}/C_L$ is minute because the sweep angle is small, and the stability of the wing is dominated by chordwise vorticity.

V. Discussion

It serves to begin this section with a brief discussion of the effect of Reynolds number on the reported stability derivative measurements and overall applicability of the current model. Angle-of-attack sweeps were repeated at $Re = 100{,}000$ and 125,000 for the forward-swept wing (planform is shown in Fig. 16) at sideslip angles of $\beta = 0$, -5, and -10 deg. Experiments at higher Reynolds numbers could not be obtained due to force balance limitations. The results are presented in Fig. 16a. Here, $-C_{l_\beta}$ is plotted against C_L up until $C_{L_{\max}}$ for each tested Reynolds number.

From Fig. 16a, both the trends with respect to C_L and magnitudes of C_{l_β} are insensitive to Reynolds number in the tested range for $C_L < 0.5$ ($\alpha \leq 10$ deg). This lift coefficient range corresponds to the applicable range of the current model [Eq. (14)]. At higher Reynolds numbers ($C_L > 0.5$), the C_{l_β} versus C_L stability curve depicts a rightward shift for the two highest Reynolds number cases relative to the lowest Reynolds number case. Figure 16b depicts lift coefficient at zero sideslip angle, C_L, (markers only) and roll moment coefficient at $\beta = -10$ deg (lined markers) for the lowest and highest tested Reynolds number cases (the intermediate Reynolds number case falls in between the two curves and is omitted). Roll moment coefficient is expressed as 10 times its actual value to use a single scale. As exhibited by Fig. 16b, the rightward shift of the lateral stability curve of Fig. 16a for the high-Reynolds-number cases is a result of the increase in lift at high angles of attack at the higher Reynolds number condition. Notably, the roll moment generated in sideslip is minimally effected by Reynolds number changes in the tested range.

The insensitivity of C_{l_β} to Reynolds number at low-to-moderate lift coefficients is consistent with previous investigations on thin low-$\mathcal{AR}$ wings at low Reynolds numbers, which report that aerodynamic loads are relatively insensitive to Reynolds number in the range 5×10^4 to 1×10^5 [7,23]. These Reynolds number effects at low-to-moderate lift coefficients are therefore expected to be largely representative of the wings tested in this study; however, additional experiments should be conducted to verify this. The insensitivity of lateral stability derivative measurements to Reynolds number are not expected to hold at higher Reynolds numbers outside of the transitional regime as the separation bubble is lost. Distinguishing the changes that occur in the lateral stability curves between the

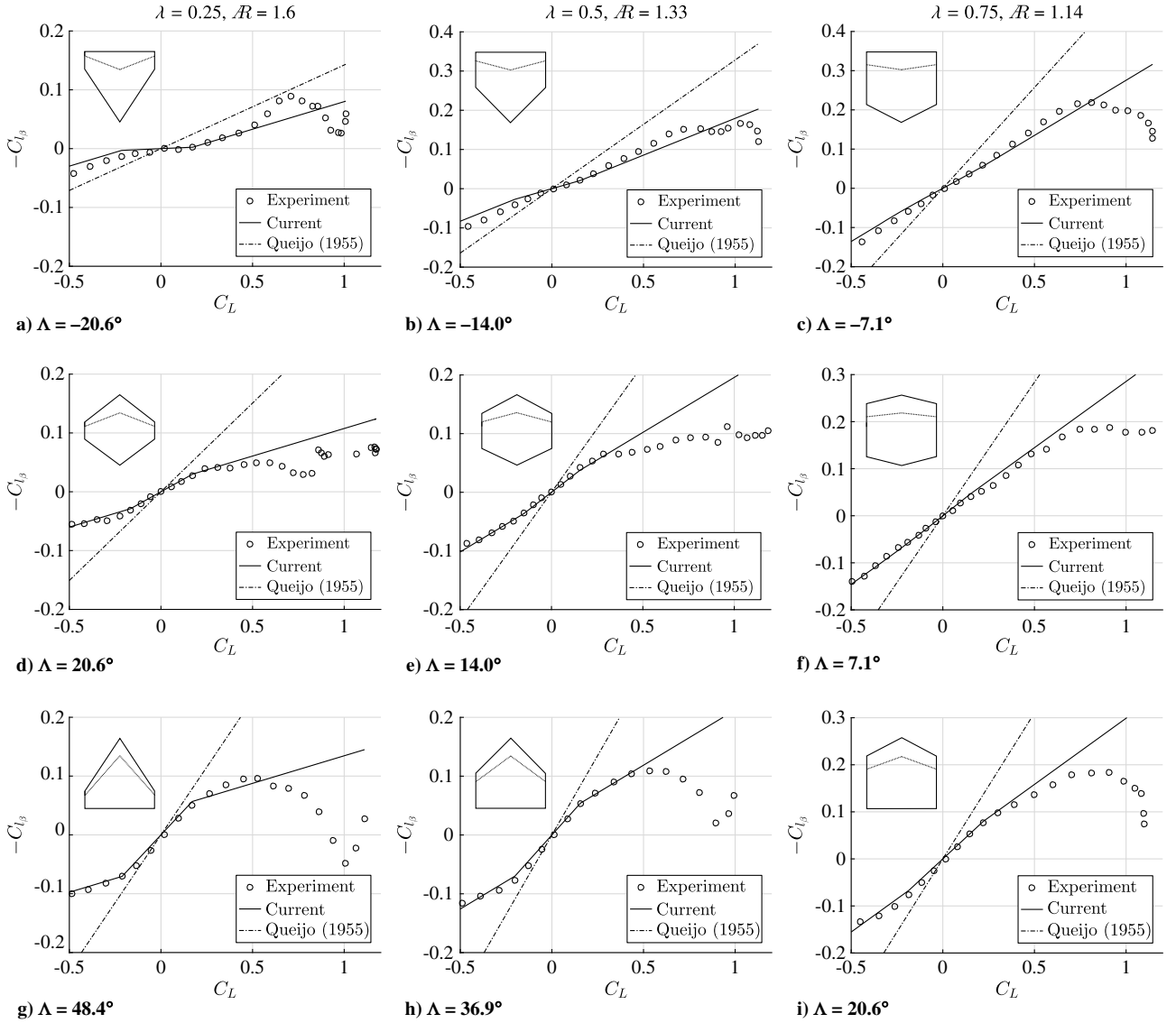

Fig. 15 Experimental measurement and theoretical prediction of the lateral stability curves for various swept tapered wings. Current theory is given by Eq. (14). Queijo theory is given by Eq. (2).

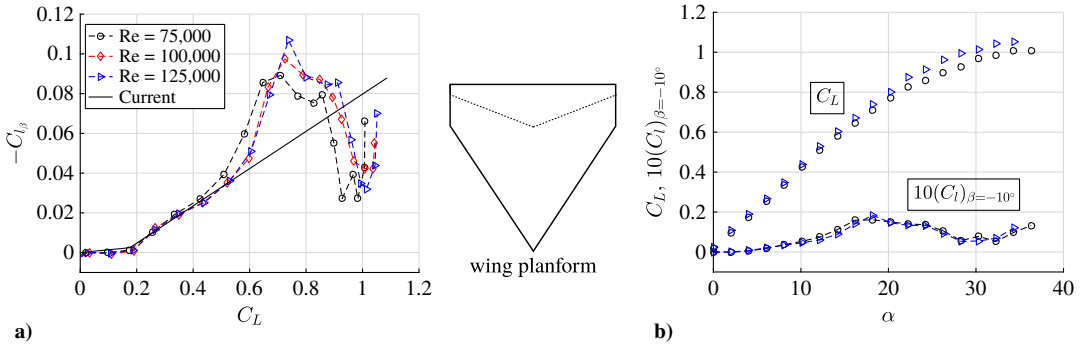

Fig. 16 Representations of a) effect of Reynolds number on the lateral stability curve, and b) lift and roll moment coefficient curves.

transitional and high-Reynolds-number flow regime remains an open research topic.

In light of the findings of this paper regarding the effect of separated transitional flows on lateral stability, several new insights into the stability and control of small-scale UAVs operating at low Reynolds numbers can be made. First, this type of aircraft is placed at an inherent disadvantage in terms of its lateral static stability due to the roll-up of the tip vortex over the wing. Here, the contribution of the wing alone to the roll stability of the full aircraft is always less than what it would be if the tip vortex roll-up occurred in the wake. To ensure the proper lateral response, designers may need to employ additional modifications to the aircraft to compensate for the lack of the roll stability contribution of the wing. One must note, however, that stability is generally antithetical to gust sensitivity. Because UAVs tend to operate in turbulent environments, the reduced lateral static stability associated with tip vortex roll-up may be favorable as

the susceptibility to uncommanded roll dynamics in turbulence is reduced.

Second, flight at angles of attack involving separated leading-edge flow can alter the aircraft lateral stability and associated roll response most notably for aircraft employing wings with significant sweep. Although this study focused on thin, flat-plate wings, modifications to the airfoil geometry of the thin wing are not expected to drastically change the general trends in the C_{l_β} curves, but more so the lift coefficient corresponding to breaks in the C_{l_β} curve. This follows the remarks of Polhamus and Sleeman, Jr., [42] regarding the stability curves of wings at high Reynolds numbers. Ultimately, a lateral controller must either be robust to modeling uncertainties associated with separated leading-edge flow or have the capability to intelligently schedule gains during flight in these regimes.

Aside from acknowledging the effects of leading-edge flow separation on roll stability, it is of interest to understand the key contributors of expedited tip vortex roll-up on thin low-$\mathcal{R}$ wings at low Reynolds numbers because this acts as a potential mechanism to control the roll response of the wing. The literature suggests that expedited tip vortex roll-up may be a result of a combination of the thinness and side-edge geometry of the wing, the low-$\mathcal{R}$ wing geometry, and the low-Reynolds-number conditions. Regarding thickness and side-edge geometry effects, sufficiently thin, sharp-edged wings fix the separation point at the edge of the wing and therefore encourage the roll-up of vorticity over thicker blunt-edged wings. Thus, designing an aircraft with a thickness and wing-tip geometry that discourages tip vortex roll-up may provide a way to increase the lateral static stability of the wing.

One can obtain an understanding of the effect of $\mathcal{R}$ on tip vortex roll-up by considering the roll-up of an elliptically loaded inviscid vortex sheet as treated by Moore [47]. From Moore [47], the characteristic time for vortex-sheet roll-up is $t_c = 2(b/2)^2/\Gamma_0$, where $b/2$ is the semispan, and Γ_0 is the characteristic root circulation for the elliptically loaded wing. Moore numerically calculated that 50% of the vorticity is in the rolled-up portion at $0.12t_c$. In the classical manner, we can transform this unsteady two-dimensional problem to a three-dimensional steady problem, here, taking the convective time as $\bar{t} = c/U_\infty$, where c is the root chord. The ratio of these two time scales (i.e., $0.12t_c/\bar{t}$) indicates the number of chord lengths traveled by the vortex sheet for which 50% of vorticity is rolled up. We can simplify the ratio as

$$\frac{0.12t_c}{\bar{t}} = 0.12\left(\frac{1}{2}\frac{U_\infty}{\Gamma_0}\frac{b^2}{c}\right) \tag{15}$$

For the elliptically loaded wing

$$\Gamma_0 = \frac{2U_\infty S C_L}{b\pi}$$

and upon combining with Eq. (15), employing the definition of $\mathcal{R} \equiv b^2/S$, and simplifying, we obtain

$$\frac{0.12t_c}{\bar{t}} = 0.12\left(\frac{\pi}{4}\frac{\mathcal{R}}{C_L}\frac{b}{c}\right) \tag{16}$$

Often a tapered wing is used to achieve a lift distribution that is nearly elliptical. From the definition of aspect ratio for linearly tapered wings, the ratio $(b/c) = (1/2)\mathcal{R}(1+\lambda)$, where λ is the taper ratio. Incorporating this definition into Eq. (16), we obtain

$$\frac{0.12t_c}{\bar{t}} = 0.12\left(\frac{\pi}{8}\frac{\mathcal{R}^2}{C_L}(1+\lambda)\right) \tag{17}$$

Equation (17) states that, at a given lift coefficient, the roll-up of vorticity occurs over a shorter number of chord lengths for low-$\mathcal{R}$ wings than high-$\mathcal{R}$ wings. From Eq. (17), the quick roll-up of the tip vortex on low-$\mathcal{R}$ wings may be further expedited for small-scale UAVs employing low-$\mathcal{R}$ wings because they tend to require higher lift coefficients to trim.

With regard to Reynolds number effects on tip vortex roll-up, Moore and Saffman [48] showed that the vortex core of an elliptically loaded viscous laminar vortex increases with downstream distance at a rate that scales with $Re^{-1/2}$, where Re is the Reynolds number based on the wing chord. Here, the vortex core grows faster with downstream distance at lower Reynolds numbers. A possible rationale for the insensitivity of lateral stability derivative measurements to Reynolds number at low lift coefficients for the wing in Fig. 16 may be attributed to its highly tapered geometry. The effects of Reynolds number on tip vortex roll-up will likely be amplified for untapered wings of low aspect ratio as the stability of the wing becomes more heavily dependent on chordwise vorticity and its modification thereof.

VI. Conclusions

Small-scale unmanned aerial vehicles (UAVs) are faced with a wide range of stability and control challenges that distinguish them from their large-scale counterparts. For one, these aircraft often incorporate low-aspect-ratio wings, which results in an inherent cross-coupling of the aircraft stability axis that enables a vertical gust or longitudinal mode to alter the vehicle's roll response. Second, these aircraft must maneuver in a low-Reynolds-number flow regime dominated by flow separation and transition, the consequences of which, in terms of aircraft stability, are just beginning to be explored. The work presented herein acts as a first step into diagnosing and incorporating low-Reynolds-number effects specifically into stability derivative predictive theory.

In this work, we show that the classical stability derivative theories of Queijo and Weissinger overpredict the lateral static stability derivative C_{l_β} on thin low-$\mathcal{R}$ wings at low Reynolds numbers. The discrepancy is attributed to the lifting-line-type vortex arrangement used to model the wing in sideslip, which does not account for tip vortex roll-up or leading-edge flow separation. To incorporate the effect of tip vortex roll-up, the vortex model of Queijo and Weissinger for the wing in sideslip was modified by the authors by reorienting the windward bound vortex in the direction of the freestream consistent with the observed flow physics of the tip vortex in sideslip. The wing in sideslip is then modeled using a single vortex element, and a linear equation for C_{l_β} is derived in terms of lift coefficient, aspect ratio, sweep angle, and taper ratio. The theory is validated against experimental low-Reynolds-number stability derivative measurements of 13 low-$\mathcal{R}$ wings with combined sweep angles and taper ratios and is shown to accurately predict C_{l_β} in the linear range across all tested wings. This work indicated that the effect of tip vortex roll-up on the wing is to reduce the lateral stability contribution of the wing (reduce the magnitude of $-C_{l_\beta}$).

The C_{l_β} curves, specifically for highly swept wings, exhibited significant nonlinear behavior at low lift coefficients $C_L \approx 0.2$, leaving the former linear predictive theory for C_{l_β} to be of little use for these wings. This is in stark contrast with the unswept wing whose stability curve remains linear up to $C_L \approx 0.7$. A classification of the stability curves, namely C_{l_β} versus C_L, was made with the assistance of particle image velocimetry measurements and surface oil-flow visualizations. The break or discontinuity in the stability ratio C_{l_β}/C_L occurring at $C_L \approx 0.2$ was deemed to be a result of the initial existence of leading-edge flow separation and subsequent reattachment over the suction surface of the wing. The low levels of circulation and associated downwash on the wing results in the separated shear layer to yield to crossflow. In this sense, the leading-edge flow does not contribute to an increment in lift due to sideslip and thus would not contribute to C_{l_β}. This effect and its influence on the break in C_{l_β}/C_L is incorporated into the model by no longer allowing the $c/4$ vortex to contribute to C_{l_β}/C_L at $C_L > 0.2$. The incorporation of this effect into the stability derivative model extends the predictive range of the previous linear theory from $C_L < 0.2$ to $C_L < 0.5$ for highly swept wings. This work indicates that the initial onset of leading-edge separation and subsequent reattachment is stabilizing for forward-swept wings, such that it increases slope $-C_{l_\beta}/C_L$, but is destabilizing for backward-swept wings because it

decreases $-C_{l_\beta}/C_L$. Furthermore, leading-edge flow reattachment does not influence C_{l_β} for unswept wings at these lift coefficients.

Acknowledgments

The authors gratefully acknowledge the partial financial support of the U.S. Air Force Office of Scientific Research and the National Science Foundation.

References

[1] Murua, J., Palacios, R., and Graham, J. M. R., "Applications of the Unsteady Vortex-Lattice Method in Aircraft Aeroelasticity and Flight Dynamics," *Progress in Aerospace Sciences*, Vol. 55, Nov. 2012, pp. 46–72. doi:10.1016/j.paerosci.2012.06.001

[2] Weissinger, J., "Der Schiebende Tragflügel bei Gesunder Strömung," Bericht S 2 der Lilienthal-Gesellschaft für Luftfahrtforschung, No. S2, 1938–1939, pp. 13–51.

[3] Queijo, M. J., "Theoretical Span Load Distributions and Rolling Moments for Sideslipping Wings of Arbitrary Plan form in Incompressible Flow," NACA TN-3605, 1955.

[4] Goodman, A., and Brewer, J. D., "Investigation at Low Speeds of the Effect of Aspect Ratio and Sweep on Static and Yawing Stability Derivatives of Untapered Wings," NACA TN-1669, 1948.

[5] Letko, W., and Goodman, A., "Preliminary Wind-Tunnel Investigation at Low Speed of Stability and Control Characteristics of Swept-Back Wings," NACA TN-1046, 1946.

[6] Linehan, T., and Mohseni, K., "Leading-Edge Flow Reattachment and the Lateral Static Stability of Low-Aspect-Ratio Rectangular Wings," *Physical Review Fluids*, Vol. 2, No. 11, 2017, pp. 23. doi:10.1103/PhysRevFluids.2.113901

[7] Shields, M., and Mohseni, K., "Effects of Sideslip on the Aerodynamics of Low Aspect Ratio Wings at Low Reynolds Numbers," *AIAA Journal*, Vol. 50, No. 1, 2012, pp. 85–99. doi:10.2514/1.J051151

[8] Katz, J., "A Discrete Vortex Method for the Non-Steady Separated Flow over an Airfoil," *Journal of Fluid Mechanics*, Vol. 102, Jan. 1981, pp. 315–328. doi:10.1017/S0022112081002668

[9] Pullin, D. I., and Wang, Z. J., "Unsteady Forces on an Accelerating Plate and Application to Hovering Insect Flight," *Journal of Fluid Mechanics*, Vol. 509, June 2004, pp. 1–21. doi:10.1017/S0022112004008821

[10] Wang, C., and Eldredge, J. D., "Low-Order Phenomenological Modeling of Leading-Edge Vortex Formation," *Theoretical and Computational Fluid Dynamics*, Vol. 27, No. 5, 2013, pp. 577–598. doi:10.1007/s00162-012-0279-5

[11] Xia, X., and Mohseni, K., "Lift Evaluation of a Two-Dimensional Pitching Flat Plate," *Physics of Fluids*, Vol. 25, No. 9, 2013, Paper 091901. doi:10.1063/1.4819878

[12] Ramesh, K., Gopalarathnam, A., Granlund, K., Ol, M. V., and Edwards, J. R., "Discrete-Vortex Method with Novel Shedding Criterion for Unsteady Aerofoil Flows with Intermittent Leading-Edge Vortex Shedding," *Journal of Fluid Mechanics*, Vol. 751, July 2014, pp. 500–538. doi:10.1017/jfm.2014.297

[13] Ol, M., and Babinsky, H., "Unsteady Flat Plates: A Cursory Review of AVT-202 Research (Invited)," *54th AIAA Aerospace Sciences Meeting*, AIAA Paper 2016-0285, 2016. doi:10.2514/6.2016-0285

[14] Xia, X., and Mohseni, K., "Unsteady Aerodynamics and Vortex-Sheet Formation of a Two-Dimensional Airfoil," *Journal of Fluid Mechanics*, Vol. 830, Nov. 2017, pp. 439–478. doi:10.1017/jfm.2017.513

[15] Carmichael, B., "Low Reynolds Number Airfoil Survey, Volume 1," NASA CR 165803, 1981.

[16] Selig, M. S., Donovan, J. F., and Fraser, D. B., *Airfoils at Low Speeds*, Stokely, Virginia Beach, VA, 1989, Chap. 1.

[17] Bastedo, W. G., and Mueller, T. J., "Spanwise Variation of Laminar Separation Bubbles on Wings at Low Reynolds Numbers," *Journal of Aircraft*, Vol. 23, No. 9, 1986, pp. 687–694. doi:10.2514/3.45363

[18] Pelletier, A., and Mueller, T. J., "Low Reynolds Number Aerodynamics of Low-Aspect-Ratio, Thin/Flat/Cambered-Plate Wings," *Journal of Aircraft*, Vol. 37, No. 5, 2000, pp. 825–832. doi:10.2514/2.2676

[19] Ananda, G. K., Sukumar, P. P., and Selig, M. S., "Measured Aerodynamic Characteristics of Wings at Low Reynolds Numbers," *Aerospace Science and Technology*, Vol. 42, April–May 2015, pp. 392–406. doi:10.1016/j.ast.2014.11.016

[20] Polhamus, E. C., "A Concept of the Vortex Lift of Sharp-Edge Delta Wings Based on a Leading-Edge Suction Analogy," NASA TN D-3767, Dec. 1966.

[21] Lian, Y., Shyy, W., Wiieru, D., and Zhang, B., "Membrane Wing Aerodynamics for Micro Air Vehicles," *Progress in Aerospace Sciences*, Vol. 39, Nos. 6–7, 2003, pp. 425–465. doi:10.1016/S0376-0421(03)00076-9

[22] Lamar, J. E., "Extension of Leading-Edge Suction Analogy to Wings with Separated Flow Around the Side Edges at Subsonic Speeds," NASA TR R-428, July 1974.

[23] Torres, G. E., and Mueller, T. J., "Low-Aspect-Ratio Wing Aerodynamics at Low Reynolds Numbers," *AIAA Journal*, Vol. 42, No. 5, 2004, pp. 865–873. doi:10.2514/1.439

[24] Cosyn, P., and Vierendeels, J., "Numerical Investigation of Low-Aspect-Ratio Wings at Low Reynolds Numbers," *Journal of Aircraft*, Vol. 43, No. 3, 2006, pp. 713–722. doi:10.2514/1.16991

[25] Okamoto, M., and Azuma, A., "Aerodynamic Characteristics at Low Reynolds Numbers for Wings of Various Planforms," *AIAA Journal*, Vol. 49, No. 6, 2011, pp. 1135–1150. doi:10.2514/1.J050071

[26] Taira, K., and Colonius, T., "Three-Dimensional Flows Around Low-Aspect-Ratio Flat-Plate Wings at Low Reynolds Numbers," *Journal of Fluid Mechanics*, Vol. 623, March 2009, pp. 187–207. doi:10.1017/S0022112008005314

[27] DeVoria, A. C., and Mohseni, K., "On the Mechanism of High-Incidence Lift Generation for Steadily Translating Low-Aspect-Ratio Wings," *Journal of Fluid Mechanics*, Vol. 813, Feb. 2017, pp. 110–126. doi:10.1017/jfm.2016.849

[28] Gresham, N. T., Wang, Z., and Gursul, I., "Self-Induced Roll Oscillation of Non-Slender Wings," *AIAA Journal*, Vol. 47, No. 3, 2009, pp. 481–483. doi:10.2514/1.42511

[29] Gresham, N. T., Wang, Z., and Gursul, I., "Low Reynolds Number Aerodynamics of Free-to-Roll Low Aspect Ratio Wings," *Experiments in Fluids*, Vol. 49, No. 1, 2010, pp. 11–25. doi:10.1007/s00348-009-0726-2

[30] Hu, T., Wang, Z., and Gursul, I., "Attenuation of Self-Excited Roll Oscillations of Low-Aspect-Ratio Wings by Using Acoustic Forcing," *AIAA Journal*, Vol. 52, No. 4, 2014, pp. 843–854. doi:10.2514/1.J052689

[31] Hu, T., Wang, Z., Gursul, I., and Bowen, C., "Active Control of Self-Induced Roll Oscillations of a Wing Using Synthetic Jet," *International Journal of Flow Control*, Vol. 5, No. 3, 2013, pp. 201–214. doi:10.1260/1756-8250.5.3-4.201

[32] Hu, T., Wang, Z., and Gursul, I., "Passive Control of Roll Oscillations of Low-Aspect-Ratio Wings Using Bleed," *Experiments in Fluids*, Vol. 55, No. 6, 2014, pp. 1752. doi:10.1007/s00348-014-1752-2

[33] Shields, M., and Mohseni, K., "Roll Stall for Low-Aspect-Ratio Wings," *Journal of Aircraft*, Vol. 50, No. 4, 2013, pp. 1060–1069; errata, Vol. 53, No. 4, 2016, pp. 1186–1188.

[34] Shields, M., and Mohseni, K., "Passive Mitigation of Roll Stall for Low Aspect Ratio Wings," *Advanced Robotics*, Vol. 27, No. 9, 2013, pp. 667–681. doi:10.1080/01691864.2013.778941

[35] Shields, M., and Mohseni, K., "Inherent Stability Modes of Low Aspect Ratio Wings," *Journal of Aircraft*, Vol. 52, No. 1, 2015, pp. 141–155. doi:10.2514/1.C032636

[36] DeVoria, A. C., and Mohseni, K., "A Vortex Model for Forces and Moments on Low-Aspect-Ratio Wings in Side-Slip with Experimental Validation," *Proceedings of the Royal Society A*, Vol. 473, No. 2198, 2017. doi:10.1098/rspa.2016.0760

[37] O'Donnell, R. S., and Mohseni, K., "Aerodynamic Parameter Estimation from Wind Tunnel Testing of a Small UAS," *2018 AIAA Atmospheric Flight Mechanics Conference*, AIAA Paper 2018-0294, 2018. doi:10.2514/6.2018-0066

[38] Linehan, T., Shields, M., and Mohseni, K., "Development, Characterization, and Validation of a Four Axis Wind Tunnel Positioning System," *52nd Aerospace Sciences Meeting*, AIAA Paper 2014-1308, 2014. doi:10.2514/6.2014-1308

[39] Coleman, H. W., and Steele, W. G., *Experimentation, Validation, and Uncertainty Analysis for Engineers*, 3rd ed., Wiley, Hoboken, NJ, 2009.

[40] Rae, W. H., and Pope, A., *Low-Speed Wind Tunnel Testing*, 3rd ed., Wiley, New York City, 1999, Chap. 10.

[41] Anderson, J. D., Jr., *Introduction to Flight*, 3rd ed., McGraw–Hill, Boston, MA, 1989, p. 397.

[42] Polhamus, E. C., and Sleeman, W. C., Jr., "The Rolling Moment Due to Sideslip of Swept Wings at Subsonic and Transonic Speeds," NACA RM-L54L01, 1955.

[43] Raffel, M., Willert, C. E., and Kompenhans, J., *Particle Image Velocimetry*, Springer–Verlag, New York, 1998, p. 195.

[44] Gursul, I., Gordnier, R., and Visbal, M., "Unsteady Aerodynamics of Nonslender Delta Wings," *Progress in Aerospace Sciences*, Vol. 41, No. 7, 2005, pp. 515–557. doi:10.1016/j.paerosci.2005.09.002

[45] DeYoung, J., and Harper, C. W., "Theoretical Symmetric Span Loading at Subsonic Speeds for Wings Having Arbitrary Plan Form," NACA TR-921, 1948.

[46] Queijo, M. J., "Theory for Computing Span Loads and Stability Derivatives Due to Sideslip, Yawing, and Rolling for Wings in Subsonic Compressible Flow," NACA TN-4929, 1968.

[47] Moore, D. W., "A Numerical Study of the Roll-Up of a Finite Vortex Sheet," *Journal of Fluid Mechanics*, Vol. 63, No. 2, 1974, pp. 225–235. doi:10.1017/S002211207400111X

[48] Moore, D. W., and Saffman, P. G., "Axial Flow in Laminar Trailing Vortices," *Proceedings of the Royal Society of London A*, Vol. 333, No. 1595, 1973, pp. 491–508. doi:10.1098/rspa.1973.0075

Y. Zhou
Associate Editor